Postprint of: Nawaz R., Haider S., Anjum M., Oad V. K., Haider A., Khan R., Aqif M., Hanif T., Khan N., Optimized photodegradation of palm oil agroindustry waste effluent using multivalent manganese–modified black titanium dioxide, ENVIRONMENTAL SCIENCE AND POLLUTION RESEARCH, Vol. 30 (2023), pp. 77850–77874

Optimized photodegradation of palm oil agroindustry waste effluent using multivalent manganese–modified black titanium dioxide

Rab Nawaz[a]*, Sajjad Haider, Muzammil Anjum[a], Vipin Kumar Oad[c], Adnan Haider[d], Rawaiz Khan[e], Muhammad Aqif[f], Tahir Hanif[g], Nasruulah Khan[h]

[a] Institute of Soil and Environmental Sciences, Pir Mehr Ali Shah Arid Agriculture University Shamsabad, Murree Rd, 46300-Rawalpindi, Pakistan.

[b] Chemical Engineering Department, College of Engineering, King Saud University, P.O. Box 800, Riyadh 11421, Saudi Arabia.

[c] Faculty of Civil and Environmental Engineering, Gdansk University of Technology, 80-233 Gdansk, Poland.

[d] Department of Biological Sciences, National University of Medical Sciences, Rawalpindi, Pakistan.

[e] Restorative Dental Sciences Department, College of Dentistry, King Saud University, Riyadh 11545, Saudi Arabia.

[f] Faculty of Materials and Chemical Engineering, Department of Chemical Engineering, Ghulam Ishaq Khan Institute, Topi 23460, Khyber Pakhtunkhwa, Pakistan.

[g] Civil and Environmental Engineering Department, The University of Alabama in Huntsville, Huntsville, AL 35899, USA.

[h] Department of Botany, University of Malakand, District Dir Lower, Chakdara 18800, Khyber Pakhtunkhwa, Pakistan

*Corresponding author Emails.: rabnawaz.utp@gmail.com; rab_17000005@utp.edu.my; Tel.: +923249832429 (Rab Nawaz)

Abbreviations

AOPs	Advanced oxidation processes	MSE	Mean square error
ANOVA	Analysis of variance	Mn	Manganese
CB	Conduction band	OPIs	Organic pollution indicators
CCD	Central composite design	PCs	Phenolic compounds
DOE	Design of experiments	POME	Palm oil mill effluent
Df	Degree of freedom	RMSE	Root mean square error
FFT	Fast Fourier transform	RSM	Response surface methodology
GA	Gallic acid	TOC	Total organic carbon
GAE	Gallic acid equivalent	TPOME	Treated palm oil mill effluent
MAD	Mean average deviation	UV	Ultraviolet
MAE	Mean average error	VB	Valence band
MAPE	Mean absolute percentage error		

ABSTRACT

This paper describes a systematic approach to optimizing and improving visible-light-driven photodegradation of treated effluent of the palm oil agroindustry (TPOME) using manganese(Mn^{3+}–Mn^{7+})-modified black titanium dioxide (Mn/$BTiO_2$) as a photocatalyst. The $BTiO_2$ was fabricated using a modified wet-chemical process, which was then wet impregnated with Mn and subjected to an hour-long calcination 300°C. The activity of Mn/$BTiO_2$ was examined for photo-assisted elimination of chemical oxygen demand (COD), phenolic compounds (PCs), color and the total organic carbon (TOC). The conditions of the photocatalytic process including the photocatalyst loading, Mn concentration, hydrogen peroxide (H_2O_2) dosage and irradiation time were optimized using design of experiments (DOE). Under optimized conditions of 0.85 g/L photocatalyst loading, 0.048 mol/L H_2O_2 dosage, 0.301wt% Mn concentration, and 204 min of visible-light treatment, exceptionally improved COD, PCs, color, and TOC removal efficiencies of 88.87%, 86.04%, 62.8% and 84.66% were obtained. According to the statistical analysis, the response variables had a high R^2 and lower RMSE, MSE, MAD, MAE and MAPE, indicating high reliability in estimating their removal from TPOME. This study established that the developed photocatalytic system has a high-level potential for the treatment of waste effluent produced by the palm oil and other

agro-industries, with the ability to abate multiple organic pollution indicators (OPIs) simultaneously.

Keywords: Manganese-doped black TiO_2, photodegradation of POME, comparative performance, design of experiments, statistical optimization

1. Introduction

In nations like Indonesia and Malaysia, the palm oil agroindustry is quickly becoming a significant industry and the foundation of the local economy. POME production has increased due to the undeniable rise in demand for edible palm oil. The yearly production of POME in Malaysia is estimated to be between 48 and 72 million tonnes (Chia et al., 2020). POME has been identified as a key polluter of the environment because of its undesirable characteristics such as high BOD_5 of 10,250−43,750 mg/L, COD of 15,000−100,000 mg/L, and PCs of more than 1000 mg/L (Iskandar et al., 2018). When the standard discharge limits stipulated by the Department of Environment Malaysia for some of the parameters were compared to the characteristics of untreated POME and TPOME (Table S1), it became clear that the pollutant concentration was still significantly higher than the permitted limit even after treatment. The high concentrations of these pollutants suggest that the methods of POME treatment currently in use fall short of the required standard.

Undoubtedly, over the years, various technologies for TPOME remediation have been explored at the laboratory scale to bring the levels of organic pollutants under the acceptable limits (Cheng et al., 2021, Aris et al., 2019, Nawaz et al., 2021), but they have some drawbacks such as high operational and maintenance costs, high energy and chemical inputs requirements and secondary pollution. In order to remediate recalcitrant pollutants in TPOME, advanced oxidation processes (AOPs) offer a desirable and sustainable alternative solution (Miklos et al., 2018, Kamyab et al., 2022, Bello and Abdul Raman, 2017). Among AOPs, the TiO_2 based photocatalysis has illustrated technical and economic feasibility for TPOME remediation

(Bello and Abdul Raman, 2017, Ng, 2021, Chowdhury et al., 2017, Moradeeya et al., 2022). Employed as a stand-alone technology, TiO_2 based photocatalysis has successfully reduced the concentrations of BOD, COD, and color of TPOME by 79, 95, and 83%, respectively, in 360 minutes of UV irradiation (Alhaji et al., 2018). When exposed to visible light, the system performed very poorly, but when exposed to UV light, it performed very well. Several methods, such as doping TiO_2 with metals (Ag, Cu, Au, Pt, Nd) (Ng et al., 2016b, Sin et al., 2020b, Cheng et al., 2015), modifying the morphology (Wong et al., 2019), heterojunction fabrication, and coupling (Sin et al., 2020a, Sin et al., 2019) have been proposed to increase the remediation efficiency of TPOME using visible irradiations. However, for industrial scale implementation, higher removal efficiencies of the various OPIs, specifically PCs using visible or solar radiations, are still required.

Fabricating black TiO_2 ($BTiO_2$) and Mn/TiO_2 could be potential approaches to improve the remediation of TPOME. The majority of researchers seem to agree that $BTiO_2$ performs better than other photocatalytic materials in a variety of applications, such as organic pollution abatement (Kouhail et al., 2022, Liang et al., 2021). For example, after only 10 minutes of visible-light irradiation, $BTiO_2$ synthesized via hydrogen plasma removed 89% of phenol from wastewater (Zhang et al., 2020). Mn doping, on the other hand, is another effective approach because Mn incorporation into TiO_2 matrix can make it efficiently utilize visible-light and significantly lessen the reunification of electron-hole pairs, thereby improving photocatalytic performance (Choi and Han, 2014). For example, Mn/TiO_2 has been shown to remove 91.7% of 2-chlorophenol after 240 minutes of solar irradiation (Sharotri et al., 2019). However, the performance of $BTiO_2$ and Mn/TiO_2 has been mainly investigated for model pollutants. As a result, it is critical to investigate $BTiO_2$ and Mn doping of TiO_2 and $BTiO_2$ for improving visible-light assisted TPOME photocatalytic remediation efficiency.

The photodegradation process parameters may be optimized using DOE and statistical modelling as a further means of enhancing TPOME's remediation. The impact of process variables such as O_2 flowrate, initial TPOME concentration, and photocatalyst loading on the remediation of TPOME has been carefully examined using a variety of machine learning and quadratic polynomial models approaches (Ng et al., 2016a, Ng et al., 2020, Jiang et al., 2020). According to optimization techniques, the optimum conditions for removing 52.52% of COD from TPOME were 70 g/L TiO_2 loading, 70 mL/L O_2 flowrate, and 250 mg/L initial COD concentration. Although the final COD removal efficiency is still low and the required TiO_2 loading of 70 g/L is very high, the models are adequate in terms of generalizability and accuracy. More importantly, no estimation or optimization of PC photodegradation in TPOME has ever used such models.

Based on the preceding discussion, the current study aimed to develop and test a photocatalytic system based on Mn/$BTiO_2$ and driven by light in the visible range for the remediation of TPOME. The synthesis of visible-light active $BTiO_2$ was carried out using a facile sol-gel process assisted by glycerol, which also served as a co-solvent and reductant. The top-performing $BTiO_2$ was further modified with Mn based on preliminary performance results. The photocatalytic process in RSM was optimized using CCD. The process performance was evaluated based on its ability to reduce OPIs in TPOME.

2. Materials and methods

2.1 Reagents and chemicals

Ammonium hydroxide (NH_4OH, 25%), Folic-Ciocalteau (F-C) reagent (≥98%), glycerol ($C_3H_8O_3$, 85%), gallic acid ($C_7H_6O_5$, 99%), hydrogen peroxide (H_2O_2, 35%), sodium carbonate (Na_2CO_3, ≥99.5%), potassium permanganate ($KMnO_4$, ≥99%), and Titanium(IV) chloride

(TiCl4, 99.9%) were purchased from Merck (Darmstadt, Germany) that were of highest purity grade and used directly.

2.2 TPOME sampling and analysis

TPOME liquid samples were gathered from a local palm oil industry's stabilization pond (final pond) in Perak, Malaysia. Sampling locations are presented in Fig. S1. To avoid changes in its properties, TPOME was kept in a cold storage at 4°C. Prior to analysis, the solid residues were removed by centrifuging the sample. The characteristics of TPOME are listed in Table S2. With gallic acid (GA) serving as a reference standard, the PCs concentration in TPOME was measure spectrophotometrically through a slightly modified F-C analytical technique. This method is used because it is quick, easy, and does not require expensive or toxic reagents (Chen et al., 2015). GA was selected as the standard because it is a pure and stable substance that is also more readily available and less costly than other options.

In a sample vial, 500 µL of diluted F-C reagent (1:4) and 100 µL of diluted TPOME were typically mixed. The mixture was then treated with 500 µL of 200 g/L Na_2CO_3 solution. To complete the reaction, the mixed solution was kept at 25−28°C for about 1 hour. A SpectroVis Plus instrument was then used to record the solution's absorbance at 765 nm. The absorbance values were converted into PCs concentrations by comparing them to the standard GA calibration (10−50 mg/L) and represented in mg/L of GAE. All measurements were taken three times and the average was reported.

With a spectrophotometer DRB5000, COD was monitored in accordance with the protocol for examining water and wastewater (Ahmad et al., 2005). The current study utilized H_2O_2 in optimization studies. However, it can affect COD tests, which could lead to an overestimation of COD measurements (Wu and Englehardt, 2012). Therefore, comparing the COD concentration in TPOME before and after the addition of H_2O_2, Eq. (1) was used to counteract the effects of residual H_2O_2 (Khraisheh et al., 2012):

$$COD_{(true)} = COD_{measured} - 0.4514 C_{H_2O_2} \quad (1)$$

where, COD_{true} is the COD concentration in TPOME before adding H_2O_2, COD_m is the measured COD after the addition of H_2O_2 and $C_{H_2O_2}$ is the H_2O_2 concentration in mg/L.

TOC was measured according to APHA Standard Method using a TOC Analyzer (TOC-VCSH SHIMADZU). A closed reflux colorimetric method was used to determine the color concentration of the TPOME before and after the reaction with help of DR3900 HACH spectrometer (Saeed et al., 2015). The color concentration was determined using platinum-cobalt (PtCo) as the standard at 455 nm.

2.3 Synthesis of $BTiO_2$ and $WTiO_2$ photocatalysts

Fig. 1 depicts a schematic of the $BTiO_2$ and $WTiO_2$ synthesis processes. A modified precipitation technique that involved hydrolyzing $TiCl_4$ in 100 mL of an aqueous glycerol, then calcining the resultant material was used to produce the $BTiO_2$ photocatalyst. Aqueous glycerol solution (1.18 mol/L) was prepared by mixing water and glycerol at 9:1 (v/v: 90:10 mL). Then approximately 18 mL of $TiCl_4$ was added to the solution drop by drop. The reaction vessel was kept in an ice bath to control the temperature of the reaction at around 5°C. To maximize the precipitation of TiO_2 particles, nearly 300 mL of 2.5 M NH_4OH were added to the reaction mixture during the precipitation process. The precipitates were centrifuged and repeatedly washed with deionized water until the washing was pH-neutral and free of chloride. The precipitates were converted to amorphous white TiO_2 powder after drying in an oven at 80°C for 12 hours. Anatase phase $BTiO_2$ was produced by calcining the dried powder for one hour at a temperature of 300°C. The $WTiO_2$ photocatalyst was synthesized in only water following the procedure as described for the synthesis of $BTiO_2$.

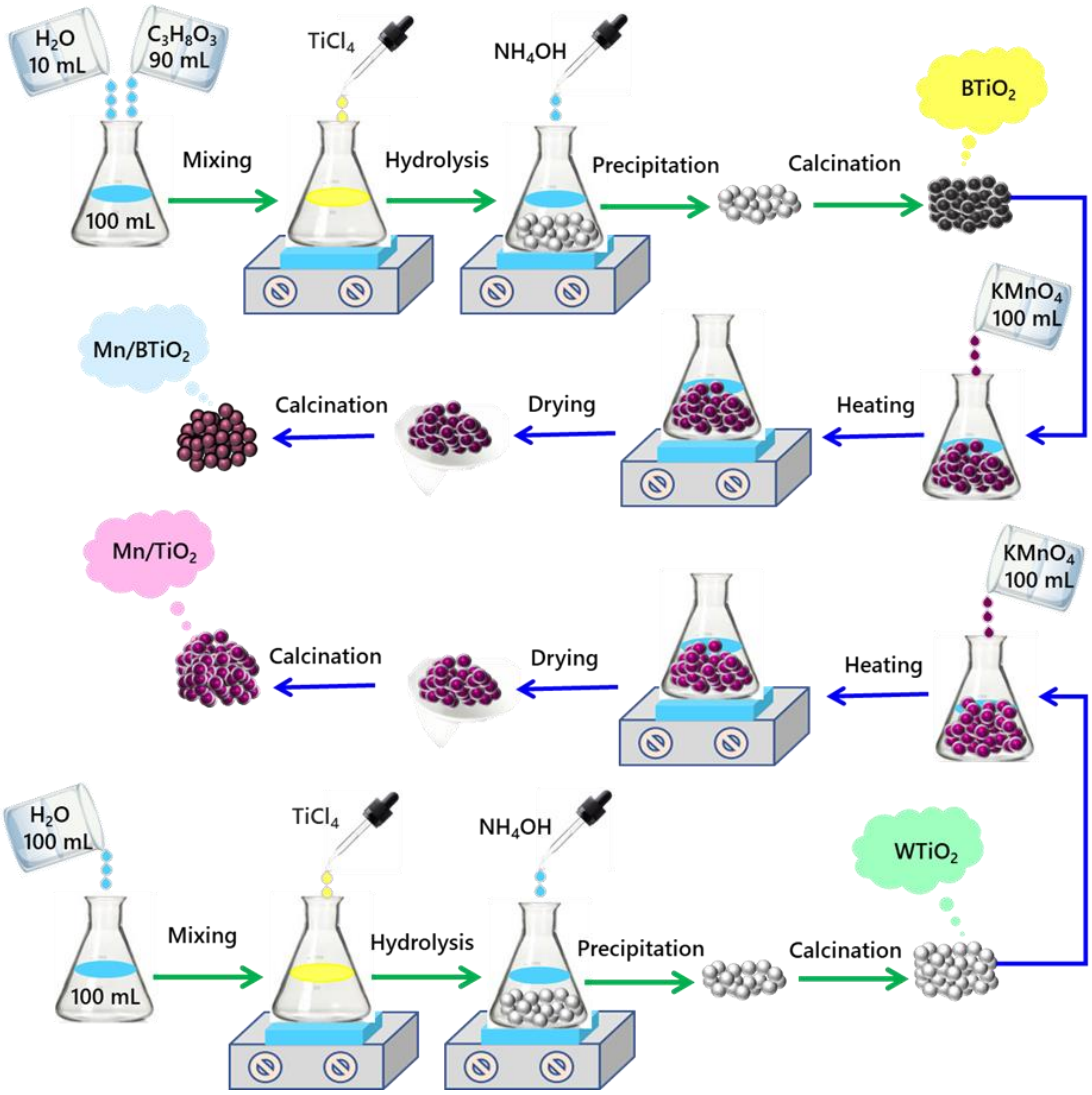

Fig. 1. Process flow diagram for the synthesis of $WTiO_2$, $BTiO_2$, Mn/TiO_2, and $Mn/BTiO_2$.

2.4 Synthesis of Mn/TiO_2 and $Mn/BTiO_2$ photocatalysts

Wet impregnation synthesis technique, which was used to prepared Mn/TiO_2 and $Mn/BTiO_2$, is shown in Fig. 1. Stock solution was prepared by dissolving 1.438 g of $KMnO_4$ in 0.1 L of deionized water. A specific quantity of the synthesised $WTiO_2$ (4.995, 4.985, and 4.975 g) was homogenised after being suspended in 100 mL of deionized water. Then, a predetermined volume from the stock solution, such as 1.0, 3.0, and 5.0 mL, was added to the homogeneous suspension to make various Mn weight percentages, such as 0.1, 0.3, and 0.5wt%, respectively. The resulting solution was heat up to 60°C until it became a slurry with constant stirring, and it was then allowed to dry for 24 hours at 80°C. The dehydrated sample

was calcined at 300°C for one hour to produce Mn/TiO_2. The Mn/$BTiO_2$ sample was prepared in the same manner as the Mn/TiO_2 sample for comparison purposes.

2.5 Characterization of the photocatalysts

XRD analysis was used to analyze the crystallinity, crystallite size, and crystalline structure of the photocatalysts. A powder X-ray diffraction spectrometer (PANalytical X'Pert3 Powder) was used to detect the XRD patterns. They were recorded in the range of 20 to 80°(2θ) with a 0.001° step size and a 2 second acquisition time per step using Cu Ka irradiation (λ=1.5406 Å). The Debye-Scherer method was employed to find the average crystallite size of the photocatalysts, as shown in Eq. (2).

$$D = \frac{K\lambda}{\beta \mathrm{Cos}\theta} \tag{2}$$

where, λ is the wavelength of the incident rays is 1.5406 Å, *K* is known as the Scherer constant, which accounts for the shape factor of particles, is typically taken to be 0.9, D is the crystallite size (nm), β is the reflection peak's full width at half maximum (FWHM), expressed in radians, and θ is the Bragg angle.

HRTEM micrographs were taken using Transmission Electron Microscope (Tecnai G2-F20 X-Twin TMP) equipped with Gatan Digital-Micrograph software. The HRTEM images were used to create 2-dimension and 3-dimension view surface plots of TiO_2 in order to determine the surface characteristics of the photocatalysts. HRTEM images were subjected to Fast Fourier Transform (FFT) analysis to distinguish crystalline from amorphous phases. The energy dispersive x-ray spectroscopy (EDX) instrument (Carl Zeiss SUPRA 55VP) was used to identify and quantify the chemical elements of the synthesized materials.

XPS analysis were carried out via Thermo Scientific spectrometer. Al Kα X-rays were employed as the source of excitation and the calibration C1s correction was applied at 284.5 eV. The Gaussian fitting was performed to obtain the XPS fitting parameters using Advantage

Software. DRUV-Vis measurements were carried out in UV-Visible spectrum (λ=200−800 nm) using UV-Vis spectrometer (Agilent Carry100). The reflectance spectra were used to calculate the bandgap energies of the materials using the KM (Kubelka-Munk) function, as shown in Eq. (3):

$$[\mathrm{F(R)h}v]^{1/2} = \mathrm{K}(\mathrm{h}v - \mathrm{E_g}) \quad (3)$$

where K has a constant value and characteristic of semiconductor, hv is the energy of the photon, and E_g is the energy gap.

The PL spectra of the materials were recoded with a spectrometer (Horiba LabRam HR Evolution). The spectra were measured at room temperature and ranged in wavelength from 300 to 700 nm with an excitation wavelength of 325 nm. The physio-sorption isotherms were measured with the Micromeritics ASAP 2020 analyzer (Micromeritcs Corps). Based on the adsorption measurement at a relative pressure (P/P_o) range of 0.1 to 1.0, the bet surface area of each sample was determined using the Brunauer, Emmett, and Teller (BET) method. For the acquisition of adsorption isotherms, the photocatalyst was placed in sample tube and cooled to −196.0°C. On the other hand, the N_2 desorption isotherms were acquired by desorption of N_2 gas from the saturated sample taking similar precautions as for adsorption process. The pore size of the TiO_2 photocatalysts were estimated from the data obtained for desorption using Barret-Joyer-Halenda (BJH) method.

3.6 Recyclability tests of the photocatalysts

In the present work, the recyclability of Mn/BTiO_2 photocatalyst, which is used in optimization study and performed better than other synthesized samples were evaluated. The Mn/BTiO_2 photocatalyst was exposed to visible spectrum range for five consecutive cycles for removing PCs and COD from TPOME. After each run, the used photocatalyst was recovered, thoroughly cleaned with deionized water, and then allowed to dry overnight before being used

in the following run. Once more suspended in TPOME solution, the recovered photocatalyst was exposed to visible light for 204 minutes.

3.7 Preliminary photocatalytic performance tests

To assess the efficiency of the synthesized photocatalysts for the photo-assisted degradation of PCs from TPOME using visible radiation, preliminary photocatalytic reactions were carried out. To achieve a photocatalyst loading of 0.5 g/L, a precisely weighted quantity of each photocatalyst ($WTiO_2$, $BTiO_2$, Mn/TiO_2, and $Mn/BTiO_2$) was suspended in 0.05 L of TPOME solution. For 30 minutes without any light, the suspension was stirred to achieve equilibrium state. After that, the suspension was subjected to visible portion of light for 180 minutes. Throughout the course of reaction, an aliquot of 1.0 mL was taken out of the photoreactor at regular intervals using a highly precise syringe. Each sample was pass through a filter (Nylon, 0.2 m) before analysis. The removal of PCs from TPOME was estimated according to the Eq. (4).

$$X\% = \frac{C_i - C_f}{C_i} \times 100\% \quad (4)$$

where Ci is the initial concentration, Cf is the final concentration of PCs, and X% denotes the degradation efficiency after a specific period of 30, 60, 90, 120, and 180 min of reaction.

3.8 Design of photodegradation experiments

Another series of photoreactions employing DOE were conducted in the presence of photocatalysts for a rigorous analysis and optimization of the independent process variables. The photodegradation experiments were designed using a statistical software (Design Expert 12.0.0, State-Eas Inc). It was also used for carrying out statistical modeling, analysis, and optimization of process variables. Independent factors such as TiO_2 loading (X_1) in g/L, H_2O_2 dosage (X_2) in mol/L, Mn concentration (X_3) in wt%, and irradiation time (X_4) in minutes were

considered in the current study. The response variables were PCs as GAE and COD removal (%) represented as Y_1 and Y_2, respectively. Other variables like light intensity, initial concentration, pH of the solution, and temperature (28-30°C) remained constant. The chosen factors were converted into dimensionless values using Eq. (5) and coded as follows A→X_1, B→X_2, C→X_3, and D→X_4. This will make it easier to compare various factors of various natures and units. This will also help reducing the possibility of statistical analysis error and make up for a lack of mathematical model fit.

$$x_i = \frac{x_i - \mathrm{X_o}}{\Delta \mathrm{X}} \tag{5}$$

where X_o is the center point value of *xi*, *xi* is the dimensionless coded value assigned to *i*th factor, and ΔX is the value assigned to the step change.

According to the CCD principle, the minimum, center, and maximum points of each input variable were designated as –1, 0, and +1, respectively. The actual and coded values as well as range of the independent variables are presented in Table 1. The CCD principle was employed during the experimental design. Table 5 depicts the experimental design matrix. The design had '2^n' fractional factorial points, '2^n' axial points, and '1' center point, with four (n) variables. Thus, 30 experiments with 10 fractional factorial points, 10 axial points, and 10 center points were carried out. In order to calculate the experimental error, reduce it, and obtain reliable results, three replicates were obtained, and the average is reported.

Table 1.

Symbols, coded values, real values, and range of independent factors.

Factors	Symbols	Coded Values	Unit	Range		
				–1	0	+1
TiO_2 loadings	A	X_1	g/L	0.4	0.9	1.4
H_2O_2-dosage	B	X_2	mole/L	0.02	0.05	0.08
Mn concentration	C	X_3	wt%	0.1	0.3	0.5
Irradiation Time	D	X_4	min	60	180	300

RSM based on CCD was used to specify the optimal levels of the independent factors and demonstrate the output nature of the response surface. Eq. (6) denotes an empirical second-order quadratic polynomial model that describes the behavior patterns of the photocatalytic system.

$$Y = \beta_o + \sum_{i=1}^{n} \beta x_i + \sum_{i=1}^{n} \beta_{ii} x_i^2 + \sum_{i=1} \times \sum_{i \neq j=1} \beta_{ij} x_i x_{ij} + \varepsilon \quad (6)$$

where, Y represents PCs and COD removal efficiency, β is the coefficient for linear effects (main effects) of the chosen variables, β_o represents the error, β_{ii} is the quadratic β_{ij} is interaction effects of the independent factors.

The analysis of variance (ANOVA), which was CCD's default method of data analysis, was used to statistically validate the model. Based on the results of the ANOVA, the complex relations between the two response variables and the four independent factors of the overall data scenario were deduced. The performance of the quadratic polynomial model fit was interpreted using the coefficient of determination (R2), which is the primary output of the multiple regression. Based on statistical tests like the Fisher's test (*F*-value), probability test (*p*-value), alpha (α=95%, 0.05) 0.05), and others, the results were evaluated. The performance of the RSM prediction was also assessed by estimating mean square error (MSE), root mean square error (RMSE), Mean average error (MAE), mean average deviation (MAD), and mean absolute percentage error (MAPE) as described in Eq.7 to 11.

$$R^2 = \frac{\sum_{t=1}^{n}(A_t - P_t)^2}{\sum_{t=1}^{n}(A_m - P_t)^2} \quad (7)$$

$$MSE = \frac{\sum_{t=1}^{n}(A_t - P_t)^2}{n} \quad (8)$$

$$RMSE = \sqrt{\frac{\sum_{t=1}^{n}(A_t - P_t)^2}{n}} \quad (9)$$

$$MAD = \frac{1}{n}\sum_{t=1}^{n}(A_t - P_t) \tag{10}$$

$$MAPE = \frac{\sum_{t=1}^{n}\left|\frac{A_t - P_t}{A_t}\right|}{100} \times 100\% \tag{11}$$

Where, A*m* represents the mean values of PCs and COD removal, A*t* represents the actual values, P*t* represents the predicted values, and *n* represents the total number of observations made for the current study.

According to the impact of the independent input variables on photocatalytic removal of PCs and COD, 3-D response surface graphs and their corresponding contour plots, and perturbation plots were produced. To determine the precise figures of the simulated values of the independent variable for the photocatalytic removal of PCs and COD from TPOME, an overlay plot was created.

3. Results and discussion

3.1. Structural properties

HRTEM was used to determine the crystal structures of the synthesized photocatalysts. All of the photocatalysts have well-resolved lattice leading edge and other features, according to analysis of HRTEM images, which were taken at a scale of 20 nm and shown in Fig. 2. The *d*-spacing, a measurement of the separation between the two lattice neighboring fringes, was approximately 0.35 nm, and it can be attributed to the 101 planes of the crystalline structure of anatase. The crystal structure was intact in the current work in both cases, either doping $WTiO_2$ and $BTiO_2$ with Mn, unlike the complete crystal destruction. However, it can be seen that when compared to $WTiO_2$, the *d*-spacing of $BTiO_2$, Mn/TiO_2, and $Mn/BTiO_2$ slightly increased. The tensile strain generated by defects like SOVs, or Ti^{3+} may be the cause of the increase in *d*-spacing (Kong et al., 2015). Since the mobility and effective mass of excitons are inversely

related, the strain induced by the defect states will essentially increase the mobility of the carriers.

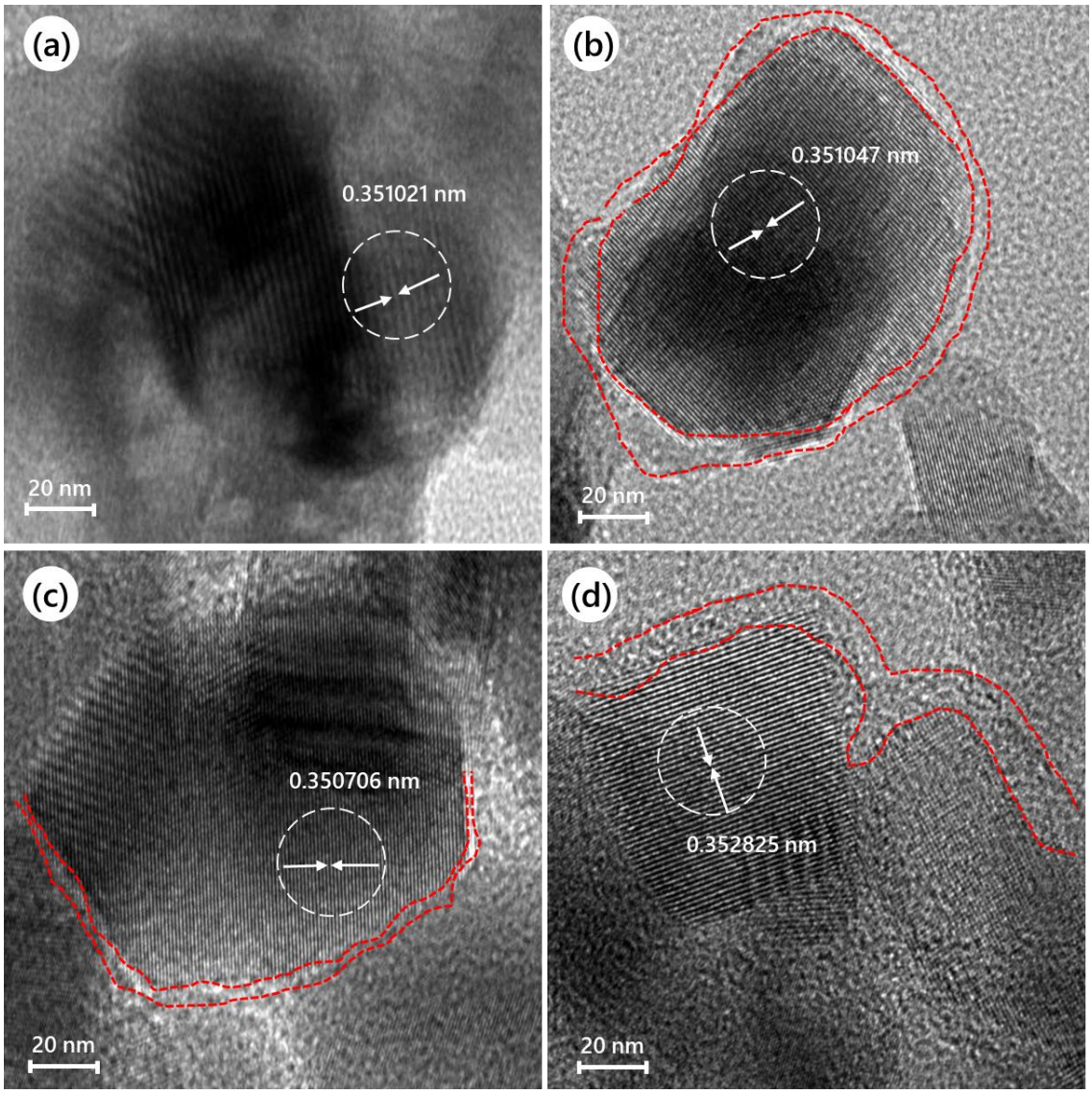

Fig. 2. HRTEM micrographs of the synthesized photocatalysts (a) $WTiO_2$, (b) $BTiO_2$, (c) Mn/TiO_2 and (d) $Mn/BTiO_2$.

Intriguingly, the crystalline core of $BTiO_2$, and $Mn/BTiO_2$ was surrounded by an amorphous shell, as shown by the red color line in Fig. 2(b−d). The core-shell structure framework was further analyzed using FFT, 3D-view surface and line analysis and the results are presented in Fig. 3. The FFT images of the particle's inner and outer surfaces are shown in the inset of Fig. 3(a). While the bright spots (each arising from Bragg reflection from a single

crystallite) in the inner zone of the FFT view confirmed that the core is crystalline, the diffuse rings in the FFT image of the particle outer region indicated that the shell is amorphous.

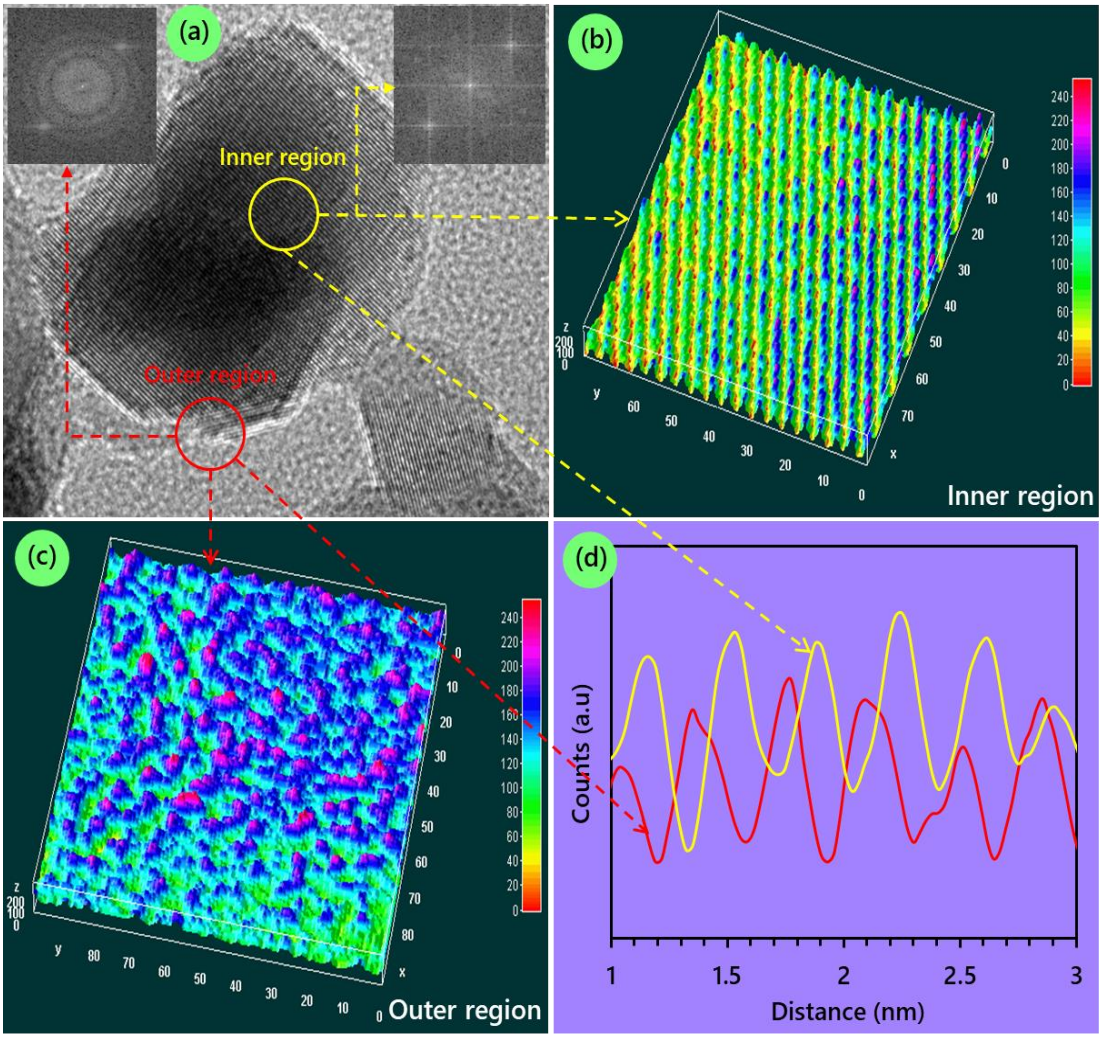

Fig. 3. (a) HRTEM image and the corresponding 3D-veiw surface plots of the (b) inner surface and (c) outer surface, and the line profiles of the inner and outer surface (d), inset of (a) FFT images of interior and outer surfaces.

The HRTEM images were further examined using 3D surface analysis for cross validation. The interior surface of the particle, which is indicated by the circular yellow line in Fig. 3(a), was used to generate the 3D view surface plots. The clear lattice fringes and appropriate atomic arrangement with flat surface in Fig. 3(b) suggest the inner core is perfectly crystalline. However, the 3D image of the particle's outer surface taken from the region indicated by the red colored circular line in Fig. 3(a) reveals a disorganized outer layer, emphasizing the

unstructured nature of the shell (Fig. 3(c)). The displacement of the interstitial Ti atom from its base and the ongoing loss of Ti atoms from the lattice, which disrupt the normal order of the atoms, lead to the formation of an amorphous structure (Tian et al., 2015, Yang et al., 2016). The line profiles created from the particle's inner and outer surfaces and displayed in Fig. 3(d) further supported the formation of the core-shell assembly with a disordered shell and crystalline core. As can be seen, the line profile created from the inner region is no longer consistent with the line profile of the outer surface.

Table 2.

Summary of the properties of the synthesized photocatalysts.

Properties	Photocatalysts				
	$WTiO_2$	$BTiO_2$	Mn/TiO_2	$Mn/BTiO_2$	P25
XRD peak position (°2θ)	25.3743	25.4136	25.3874	25.3823	—
Crystallite size (nm)	47.66	50.87	48.01	47.89	55.10
FWHM	0.3883	0.1872	0.4605	0.5117	0.2558
d-spacing (Å)	0.351021	0.351047	0.350706	0.352825	0.3509
Absorption wavelength (nm)	410	450	>650	>650	388
Bandgap (eV)	3.16	2.96	2.42	2.29	3.20
Surface area (m^2/g)	154.51	99.88	116.41	94.03	50
Pore volumes (cm^3/g)	0.198	0.161	0.210	0.159	—
Pore size (nm)	4.35	3.06	5.05	5.03	—

The XRD diffractogram of the photocatalyst shown in Fig. 4(a) revealed that all the synthesized photocatalyst are pure anatase phase indicated by the sharp diffraction peaks around 25° (2θ). A noticeable difference between $WTiO_2$ and other photocatalysts was observed when their intense diffraction peak (101 plane) was magnified as depicted in Fig. 4(b). The diffraction peak shifted to higher angle in $BTiO_2$ and $Mn/BTiO_2$, which may be attributed structural deformation due to an expansion in *d*-spacing (Xia and Chen, 2013, Kunnamareddy et al., 2023). When compared to $WTiO_2$, the 101 peak of $BTiO_2$ did, in fact, shift to a higher angle, moving from 25.3743 to 25.4136° (Table 2). This result is in line with earlier research, which showed that black TiO_2 and Mn/TiO_2 diffraction peaks (101 plane) shifted to higher angles than pure TiO_2 (Ullattil and Periyat, 2015). In contrast, yellow TiO_2

has been found to have the diffraction peak shift to a lower angle (Bi et al., 2020). The discrepancy between these results and those from prior studies could be attributed to the use of different types of synthesis techniques and starting reagents.

The anatase phase was intact even if $WTiO_2$ or $BTiO_2$ were impregnated with Mn. No peaks representing oxides of Mn such as Mn_3O_4 or Mn_2O_3 were detected in the XRD patterns suggesting the existence of Mn as impurity (Bousiakou et al., 2022). Due to the close proximity of the ionic radii of the Ti^{4+} (0.06 nm) and Mn^{4+} (0.053 nm), as well as the fact that neither HRTEM nor XRD revealed any evidence of the Mn oxides, it is also likely that Mn is distributed evenly in Mn/TiO_2 and $Mn/BTiO_2$ matrices. $WTiO_2$ and $BTiO_2$ were both doped with Mn, yet there was no meaningful difference in the XRD patterns in either case.

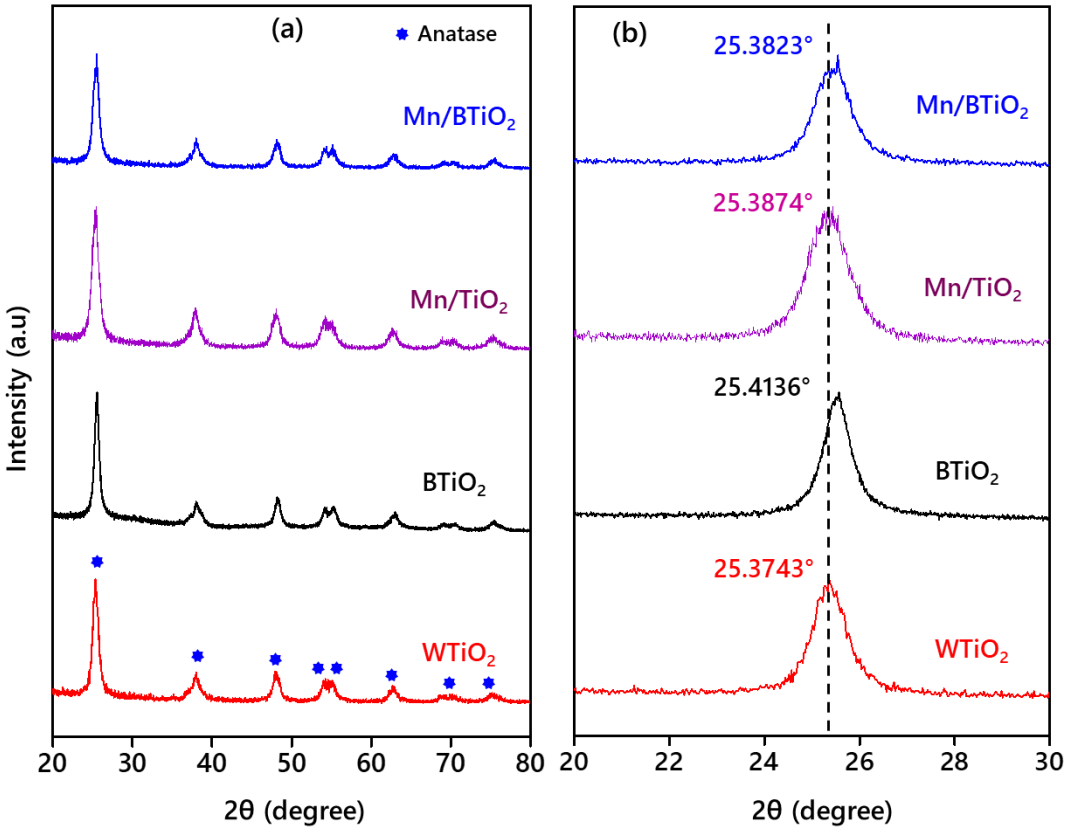

Fig. 4. (a) XRD diffractogram and (b) enlarged XRD (101) peaks of the synthesized photocatalysts.

3.2 Electronic and optical properties

Deconvoluted Ti2p XPS spectra of $WTiO_2$ are displayed in Fig. 5(a). The $Ti2p_{3/2}$ peak's binding energy (BE) was 459.54 eV, while the $Ti2p_{1/2}$ peak's BE was 465.18 eV. These peak positions represent the typical Ti^{4+}—O bonds in the common crystalline phase of anatase (Shvab et al., 2017). The $WTiO_2$ O1s spectrum is depicted in Figure 6(a). The two peaks that were discernible at BE values of 530.81 and 532.15 eV, respectively, are due to lattice O in TiO_2 and surface adsorbed OH. The $Ti2p_{3/2}$ and $Ti2p_{1/2}$ peaks of $BTiO_2$ had BE values of 458.85 and 463.58 eV, respectively, as shown in Fig. 5(b). The peaks may have shifted to their lower BE positions due to an expansion in the Ti—O bond's length brought on by the action of defect species (Pan et al., 2013). There was an extra shoulder peak in the Ti2p XPS spectrum of $BTiO_2$ at a lower BE of 457.51 eV, which is explained by lower oxidation state Ti^{3+} (Bharti et al., 2016). Three peaks at BE 530.32, 531.76, and 532.61 eV in the O1s spectrum of $BTiO_2$ have been identified as the lattice O in TiO_2, suboxide, and OH, respectively.

The XPS Ti2p spectra for Mn/TiO_2 are shown in Fig. 5(c). The deconvoluted spectra revealed two peaks at BE of 459.73 and 465.76 eV that correspond to the $Ti2p_{3/2}$ and $Ti2p_{1/2}$ orbital doublets and are typical of anatase phase TiO_2. The results are in line with the XRD results shown in Fig. 4 and demonstrate that the synthesized Mn/TiO_2 phase was unaffected by Mn doping. It is important to understand that the $Ti2p_{3/2}$ peak positive shift to the high BE is an indication of the lattice distortion brought on by the inclusion of Mn into the TiO_2 matrix. Fig. 6(c) depicts the Mn/TiO_2 O1s spectra. Two overlapping peaks at BE 532.46 and 533.37 eV are visible in the spectra. Lattice oxygen and oxygen vacancies, respectively, were responsible for both of these peak positions. (Qiu et al., 2016). The Ti2p spectra of $Mn/BTiO_2$ in Fig. 5(d), on the other hand, showed two major peaks at BE of 460.00 and 465.51 eV and a shoulder peak at 458.72 eV, which, respectively, represent the Ti^{4+} ($Ti2p_{3/2}$ and $Ti2p_{1/2}$) and Ti^{3+} ($Ti2p_{3/2}$) states.

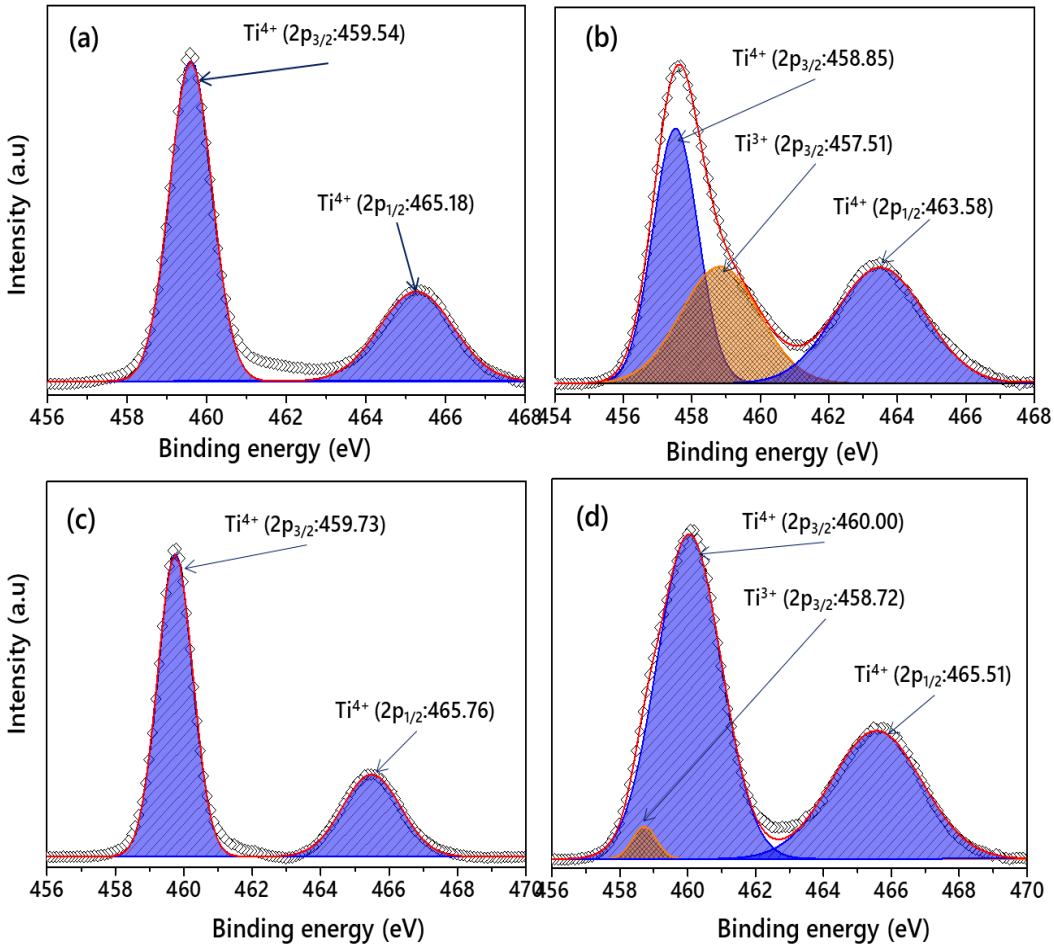

Fig. 5. XPS spectra Ti2p of deconvoluted peaks of (a) $WTiO_2$, (b) $BTiO_2$, (c) Mn/TiO_2, and (d) $Mn/BTiO_2$.

The core level XPS spectra of the photocatalysts in Fig. S2 demonstrate the presence of Mn. EDX was also used to cross validate the existence of Mn in the TiO_2 matrix. The EDX spectra and mapping of the photocatalyst are shown in Fig. S3. The EDX mapping revealed the presence of Ti, Mn, O, and C in the $Mn/BTiO_2$ and the even distribution of the Mn throughout the TiO_2 matrix. It was found that the experimental Mn concentration of 0.48wt% matching closely with the theoretical Mn concentration of 0.5wt%. On the surface of $Mn/BTiO_2$, the valence state of Mn was examined using XPS analysis.

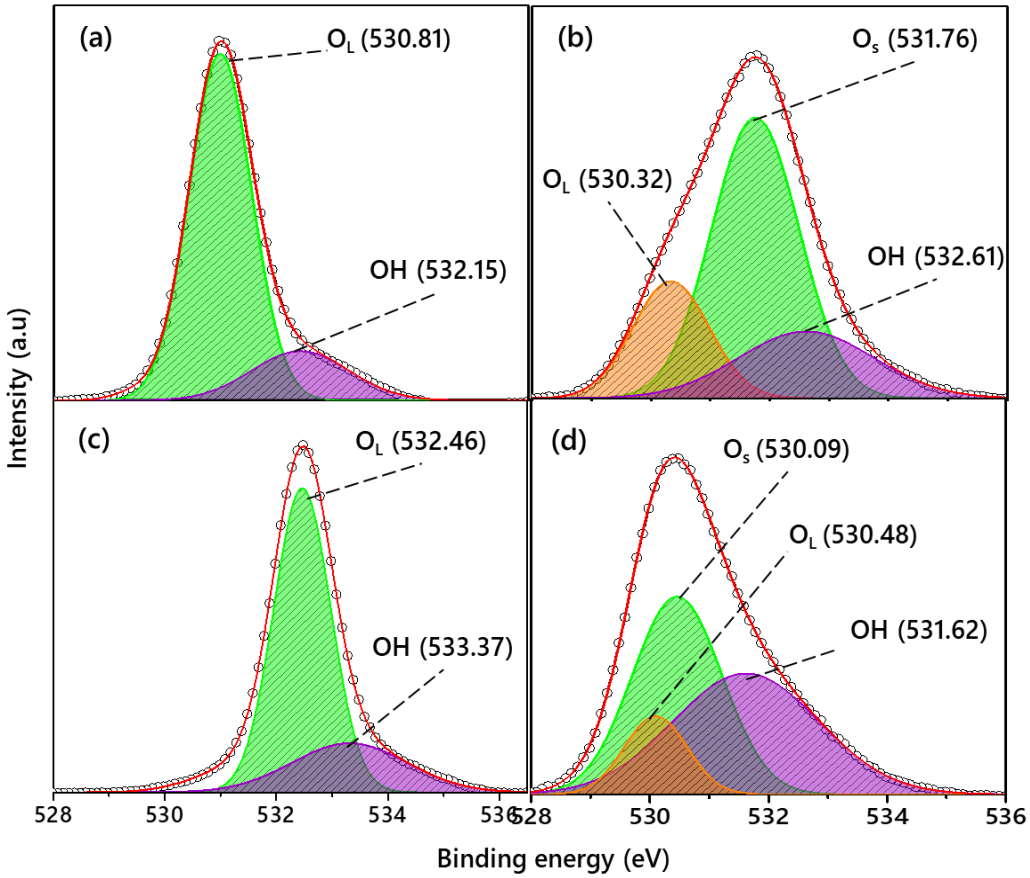

Fig. 6. Deconvoluted O1s XPS spectra of (a) $WTiO_2$, (b) $BTiO_2$, (c) Mn/TiO_2, and (d) $Mn/BTiO_2$.

The $Mn2p_{3/2}$ peak was split into four separate peaks, each of which corresponded to a different electronic state of Mn as shown in Fig. 7(d). The peaks correspond to Mn^{3+}, Mn^{4+}, Mn^{6+}, and Mn^{7+} at energies of 642.68, 643.98, 645.12, and 646.23 eV, which agrees with the theoretical values found in the literature (Zhang et al., 2021, Sun et al., 2020). The absence of metallic Mn or Mn^{2+} peaks in the spectra suggests that neither substance is present in the sample. The coexistence of numerous states of Mn on the surface TiO_2 has a major role in the emergence of surface oxygen because the multivalent-valence state of the metal can encourage oxygen maneuverability in the semiconductor oxides (Bhardwaj and Pal, 2020, Sharotri et al., 2019).

Fig. 7(a) displays a comparison of the high resolution C1s spectra of Mn/TiO_2 and $Mn/BTiO_2$. The $Mn/BTiO_2$ C1s peak has evidently been moved to a higher BE. The shift of

the C1s peak to higher BE is in harmony with the Ti2p and O1s peaks, which both moved towards higher BE. These findings imply that the addition of Mn to the matrix of the $BTiO_2$ alters its chemical environment. To better comprehend the photocatalyst chemical surroundings, the C1s spectra of the samples were deconvoluted. The Mn/TiO_2 high resolution deconvoluted C1s spectra are shown in Fig. 7(b). The peaks were found at a BE of 285.10, 286.08, and 289.32 eV, and they are attributable to (C—C) with sp2 hybridization, coke carbon, and C atoms, respectively (Piątkowska et al., 2021).

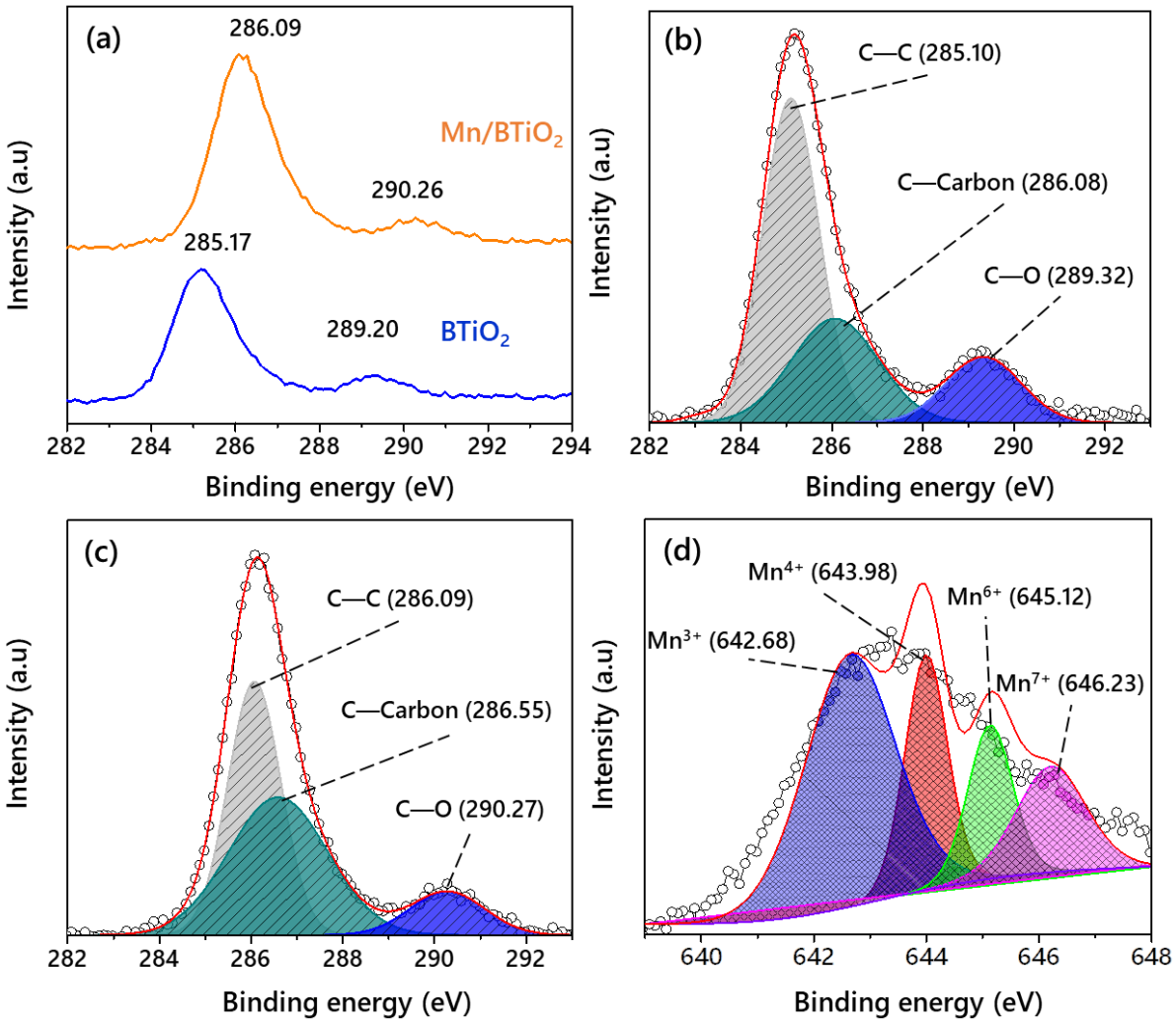

Fig. 7. (a) Comparison of C1s spectra of Mn/TiO_2 and $Mn/BTiO_2$, deconvoluted C1s spectra of (a) Mn/TiO_2 and (b) $Mn/BTiO_2$ and (d) deconvoluted Mn2p spectra of the $Mn/BTiO_2$.

To gain insight into the optical characteristics of the synthesized photocatalysts, DRUV-Vis analysis was carried out. The photocatalysts' UV-visible spectra are shown in Fig. 8(a). $WTiO_2$ is only capable of absorption in the near ultraviolet region, in contrast to $BTiO_2$, Mn/TiO_2, and $Mn/BTiO_2$ which are all capable of absorption in the visible spectrum. After doping the $WTiO_2$ and $BTiO_2$ with Mn, the light absorption was clearly promoted into the visible region. (Choi et al., 2002) explained that a charge exchange between Mn (d electrons) and VB or CB, or a d-d changeover in the crystal field, is what's to intensify the visible light absorption. This is further supported by theoretical research that showed that the creation of intermediate bands into the forbidden gap and the overall reduction of the band gap caused by the replacement of Mn for Ti in the TiO_2 lattice resulted in a dramatic red-shift of the optical absorption edge (Lu et al., 2012). The occupation of the orbital by an unpaired valence electron and the resulting spin polarization give rise to the intermediate bands. Since gap state formation is made easier by orbital occupation, Mn doped material exhibits intermediate bands (Liang and Shao, 2019). These bands serve as steppingstones to increase the effective optical absorption.

The *T*-plot in Fig. 8(b) was used to estimate the bandgap energies. The bandgap of $BTiO_2$ (2.96 eV) is lower than that of $WTiO_2$ (3.16 eV). When Mn was doped into both photocatalysts, their bandgap energies were significantly lowered to 2.42 and 2.29 eV, which may be associated to the curved transitional bands inside the bandgap (Xia et al., 2012). The increased electron concentration in the shape of Mn cations, which results in the hybridization of the d-states of Mn with the CB edge of TiO_2, may be the reason why the bandgap has shrunk. This bandgap narrowing does not, however, ensure increased photocatalytic activity. Instead, narrow bandgaps that increase light absorption and decrease electron and hole recombination are essential for improving photocatalytic activity.

To better comprehend the behavior of charges recombination, the PL spectra of the synthesized photocatalysts were measured and displayed in Fig. 8(c). The fact that the peak intensities of the modified samples were noticeably lower than those of $WTiO_2$ suggesting that the recombination of photoexcited electron-hole has been significantly reduced (Moya et al., 2015). $BTiO_2$ and $Mn/BTiO_2$ were further studied using EIS to determine the rate of electron and hole recombination and the resistance to charge transfer in them. Fig. 8(d) displays the EIS spectra revealing higher separation, a slower rate of recombination, and less resistance to charge transfer are all indicated by smaller semicircle radius (Sigcha-Pallo et al., 2022) in the spectrum of $Mn/BTiO_2$ compared to $BTiO_2$.

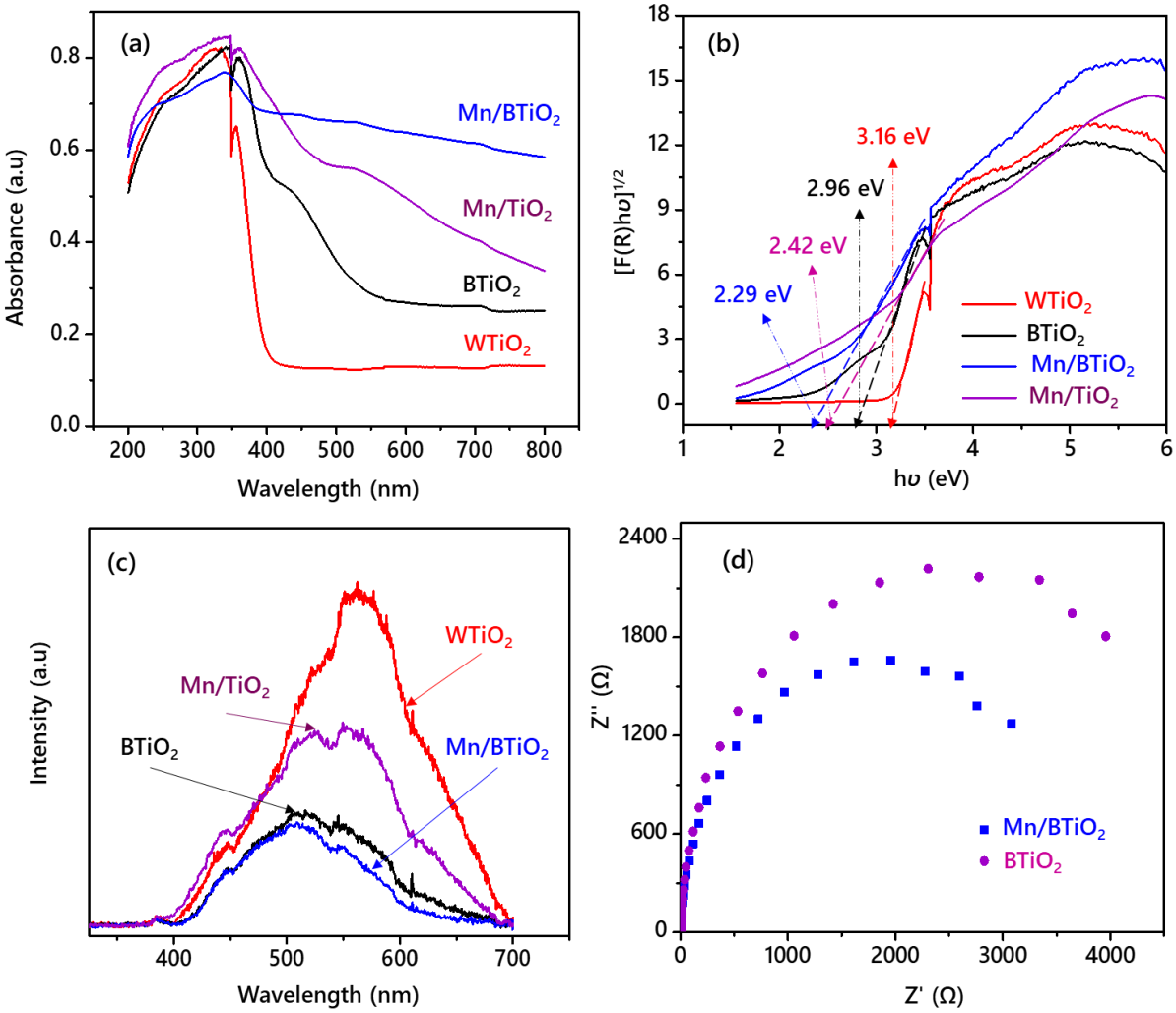

Fig. 8. UV-Visible absorption spectra, T-plot of the bandgaps, PL of the synthesized photocatalysts, and Pl spectra of the $BTiO_2$ and $Mn/BTiO_2$.

3.3 Preliminary photodegradation studies

To determine the efficacy of the photocatalysts for the degradation of PCs from TPOME, preliminary photodegradation experiments were conducted. Fig. 9(a) displays the normalised concentration of PCs in TPOME following 180 minutes of photocatalytic treatment under visible light. The $WTiO_2$ was capable of eliminating 28.96% of PCs with an apparent removal rate constant of 1.4×10^{-6} min^{-1}. With a higher apparent removal rate constant of 2.8×10^{-6} min^{-1}, the PCs removal efficiency rose to 48.30% when $BTiO_2$ was used as the photocatalyst. $WTiO_2$ is less efficient than all other photocatalyst at removing PCs despite having a larger surface area than the other samples (Table 2). This is due to the fact that the wide bandgap of 3.16 eV of $WTiO_2$ prevents it from utilising existing light in the visible spectrum. In addition, $WTiO_2$ has higher charged species recombination and a shorter lifespan (Fig. 8c), which may also contribute to its poor performance in the visible light spectrum.

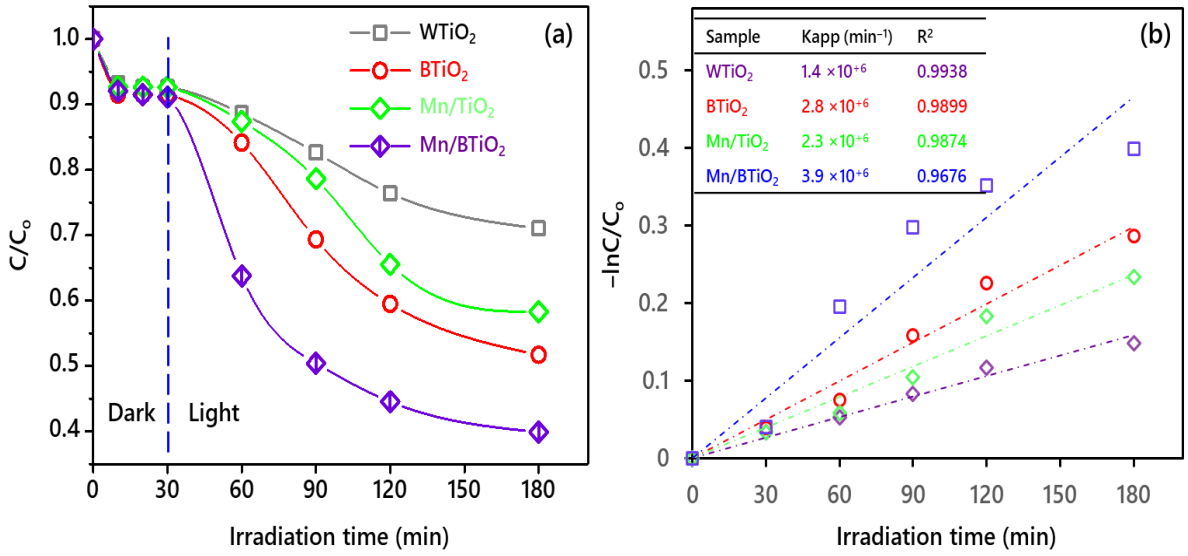

Fig. 9. (a) Normalized concentration of PCs after 180 min of photocatalytic treatment and and (b) corresponding pseudo first order kinetic plots.

The improved PCs removal by $BTiO_2$ is a result of both the presence of Ti^{3+} species and the material's distinctive core-shell structure. The shell might provide the active sites for effective PC adsorption, whereas the sustained Ti^{3+} species within the crystalline core make up

an inter-band energy level. Since $BTiO_2$ has a lower bandgap than $WTiO_2$, the electrons can easily be excited from the Ti^{3+} centres to the CB with the aid of visible light absorption, and the shell acts as a trap for the electrons to minimise their interaction with the hole (Rostami et al., 2022). As a result, free electrons and holes are available for a longer period of time to further react with atomic oxygen and water to produce reactive radicals that attack and degrade PC molecules.

The removal efficiency of PCs was further enhanced by doping Mn into the $WTiO_2$, reaching 41.69% with an increase in apparent rate constant to 2.3×10^{-6} min^{-1}. When the $BTiO_2$ was doped with Mn, the PC removal gradually increased to 60.12%, with the highest apparent rate constant being 3.9×10^{-6} min^{-1}. The increased removal of PCs by Mn/TiO_2 and $Mn/BTiO_2$ over $WTiO_2$ may be attributable to the addition of intermediate curvy bands within the bandgap that make it easier for electrons and holes to be separated under the visible light energy (Deng et al., 2011). Interband levels introduced by Mn also extend the life span of charged species, accelerating the elemination of PCs. It should be noted that Mn/TiO_2 is less effective at removing PCs than $BTiO_2$. Mn ions, however, add additional positive charge to the surface of $WTiO_2$, increasing the repulsive interaction between the particles and making Mn/TiO_2 highly stable in wastewater treatment applications (Bhardwaj and Pal, 2020). Higher oxidation state Mn (>2+) impurities enhance TiO_2 capacity for light absorption, pollutant adsorption, and subsequent photodegradation in addition to providing stability (Choi et al., 2010).

3.4 Process optimization for photodegradation of TPOME

Since the preliminary results of removing PCs from TPOME confirmed the higher performance of $Mn/BTiO_2$, Therefore, the photocatalytic process for PCs and COD removal from TPOME matrix optimization studies used $Mn/BTiO_2$. Then the optimized process was also tested for TOC and color removal from the TPOME.

3.4.1 Model fit summary statistics and statistical significance

Analysis of variance (ANOVA) was used to assess the model's statistical significance and is shown in Table 3. Overall model *p*-values for PCs and COD elimination were 0.0001, which was less than the 0.05 level of significance. So, it was determined that there was a relationship between the independent variables and the outcome variables, rejecting the null hypothesis. Because of this, the PCs and COD removal are significantly impacted by the full quardritic model of the selected independent factors. The fact that the *p*-value for the factors linear term is below the level of significance suggests that the factors have a significant impact on PCs and COD removal (Table S3).

Table 3.

ANNOVA output table for COD and PCs as GAE removal.

Source	Sum of squares	Mean square	df	*F*-value	Prob>*F*/*P*-values	Remarks
For PCs as GAE						
Model	4669.76	333.55	14	64.78	0.0001	Significant
Lack of fit	30.30	3.03	11	1.16	0.0507	Insignificant
For COD						
Model	3424.41	244.60	14	63.46	0.0001	Significant
Lack of fit	45.90	4.59	10	3.28	0.1790	Insignificant

Regarding PCs and COD removal, the *p*-value for the interactions of the independent factors is found to be significant. The *p*-values for the PCs (0.0507) and COD (0.1790) removal models were greater than the level of significance, there is no lack-of-fit in these models. As a result, the quadratic models with the independent variables shown in Eqs. 12 and Eq. 13 have a considerable impact on the photodegradation of PCs (Y_1) and COD (Y_2) removal from TPOME. The direction and strength of the relationship were denoted by the sign and value of the coefficients, respectively.

The model summary output shown in Table 4 is used to run the practical significance test. While the adjusted R^2 values for the response variables were 98% and 97%, the observed R^2

values for PCs and COD were 99% and 98%, respectively. These findings suggest that the model's parameters are very effective at explaining variation in PCs and COD removal. Furthermore, high R^2 values for both the response variables ensure a satisfactory agreement between the observed and predicted PCs and COD removal and a good model fit (Glaz and Yeater, 2020) . As a result, the model has strong practical relevance.

$$(Y_1) = 87.66 + 0.032A - 0.18B + 1.21C + 2.75D - 0.37AB - 1.97AC - 4.14AD - 0.93BC + 0.028BD - 0.29CD - 5.69A^2 - 4.35B^2 - 13.35C^2 - 13.23D^2 \quad (12)$$

$$(Y_2) = 93.53 - 1.03A - 1.08B - 0.84C + 2.81D - 0.29AB - 3.16AC - 3.16AD + 1.24BC - 0.27BD + 0.023CD - 7.22A^2 - 3.77B^2 - 14.69C^2 - 3.75D^2 \quad (13)$$

Table 4.

RSM output model fit summary for COD and PCs as GAE removal.

Statistical key figure	Acronym	GAE removal	COD removal
Predicted residual error sum of square	PRESS	321.26	329.52
Coefficient of determination	R^2	0.99	0.98
Mean average percentage error	MAPE	0.952	0.046
Mean average deviation	MAD	2.112	1.560
Root mean square error	RMSE	2.542	1.857
Mean average error	MAE	2.110	1.506
Mean square error	MSE	6.459	3.448
Coefficient of variance	C.V.	2.58	2.77
Standard deviation	St. Dev.	1.71	21.96
Adequate precision	A.P.	37.60	25.78
Predicted – R^2	Pre. R^2	0.95	0.90
Adjusted – R^2	Adj. R^2	0.98	0.97
Mean	Mean	66.28	76.10

Table 5.

Experimental design matrix (DOE), experimental and predicted values for PCs as GAE and COD removal from TPOME.

Run no.	A: TiO_2 loading (g/L)	B: H_2O_2 dosage (mol/L)	C: Mn conc. (wt%)	D: Time (min)	PCs as GAE removal (%)		COD removal (%)	
					Experimental	Predicted	Experimental	Predicted
1	0.4	0.02	0.5	60	59.21	61.98	76.17	73.62
2	1.4	0.08	0.1	300	52.41	51.99	61.64	59.15
3	1.4	0.02	0.1	60	54.86	53.05	64.26	63.84
4	0.9	0.05	0.3	180	57.31	54.48	69.81	69.79
5	1.4	0.08	0.5	60	59.27	56.76	74.19	71.05
6	0.4	0.08	0.5	300	48.51	50.27	62.89	60.74
7	0.4	0.08	0.1	60	88.79	89.56	94.58	93.67
8	1.4	0.02	0.5	300	90.13	89.56	93.25	93.73
9	0.9	0.05	0.3	180	48.94	52.39	58.97	59.54
10	0.4	0.02	0.1	300	43.29	43.66	55.17	55.09
11	0.9	0.05	0.3	180	64.73	62.63	70.48	73.28
12	0.4	0.02	0.5	300	52.79	54.42	64.39	65.12
13	1.4	0.02	0.1	300	48.52	51.45	68.41	69.58
14	0.4	0.08	0.1	300	57.21	57.30	63.78	66.46
15	1.4	0.02	0.5	60	41.34	40.68	56.32	58.62
16	0.9	0.05	0.3	180	53.19	54.64	58.43	59.27
17	1.4	0.08	0.5	300	87.34	88.71	91.67	93.53
18	0.4	0.08	0.5	60	48.12	48.31	57.13	58.35
19	1.4	0.08	0.1	60	51.36	47.96	59.81	62.16
20	0.4	0.02	0.1	60	86.13	88.79	93.69	93.62
21	0.9	0.05	0.3	60	72.34	74.16	90.45	92.59
22	0.4	0.05	0.3	180	75.12	80.46	88.73	90.83
23	0.9	0.05	0.3	300	68.45	68.66	90.13	86.97
24	0.9	0.05	0.3	180	74.23	72.49	77.18	78.00
25	0.9	0.05	0.5	180	89.93	84.63	93.16	93.54
26	0.9	0.05	0.1	180	87.46	84.64	94.76	93.91
27	0.9	0.08	0.3	180	81.61	78.98	85.46	85.28
28	1.4	0.05	0.3	180	83.43	80.13	91.77	87.67
29	0.9	0.05	0.3	180	74.25	78.91	88.15	87.33
30	0.9	0.02	0.3	180	66.31	68.07	81.49	79.68

Table 3 displays the Fisher's (*F*-values) for the models. *F*-values of 64.78 and 63.46 indicated that the models were significant for effective PCs and COD removal, respectively. The percentage of models with large *F*-values that are susceptible to noise is less than 1% (0.01). In other words, there is a strong argument that the models were accurate and that there is a very low likelihood that the large *F*-values are the result of pure chance (*p*-value=0.0001). Table S4 contains the detailed ANOVA table with the *p*-values for each model term. The adequate precision (AP), which assesses "signal to noise ratio," was discovered to be 37.60% and 25.78%, respectively, for PCs and COD removal (Table 4). When the AP value exceeded 4, it meant that both modes could be used to maneuver in the space that had been previously defined by the CCD/RSM.

It is crucial to assess the reliability and applicability of CCD by calculating important statistical indicators like MSE, RMSE, MAD, MAE and MAPE values which should be as small as possible, and R^2 values should be close to 1, for ideal model fitting (Ateia et al., 2020). The likelihood of error in the estimation of PCs and COD removal from TPOME increases with higher values of statistical indicators. The lower RMSE values of 2.542 and 1.857 for PCs and COD elimination from TPOME showed no departure from the quadratic polynomial model, demonstrating the reliability of the RSM. Low RMSE and high R^2 values for both responses in the fitting analysis results shown in Table 4 imply that the CCD used can more accurately predict and optimize the photodegradation of PCs and COD. Lower values for MAPE, MSE, and MAE as well as higher R^2 values were observed, indicating a lower probability of error.

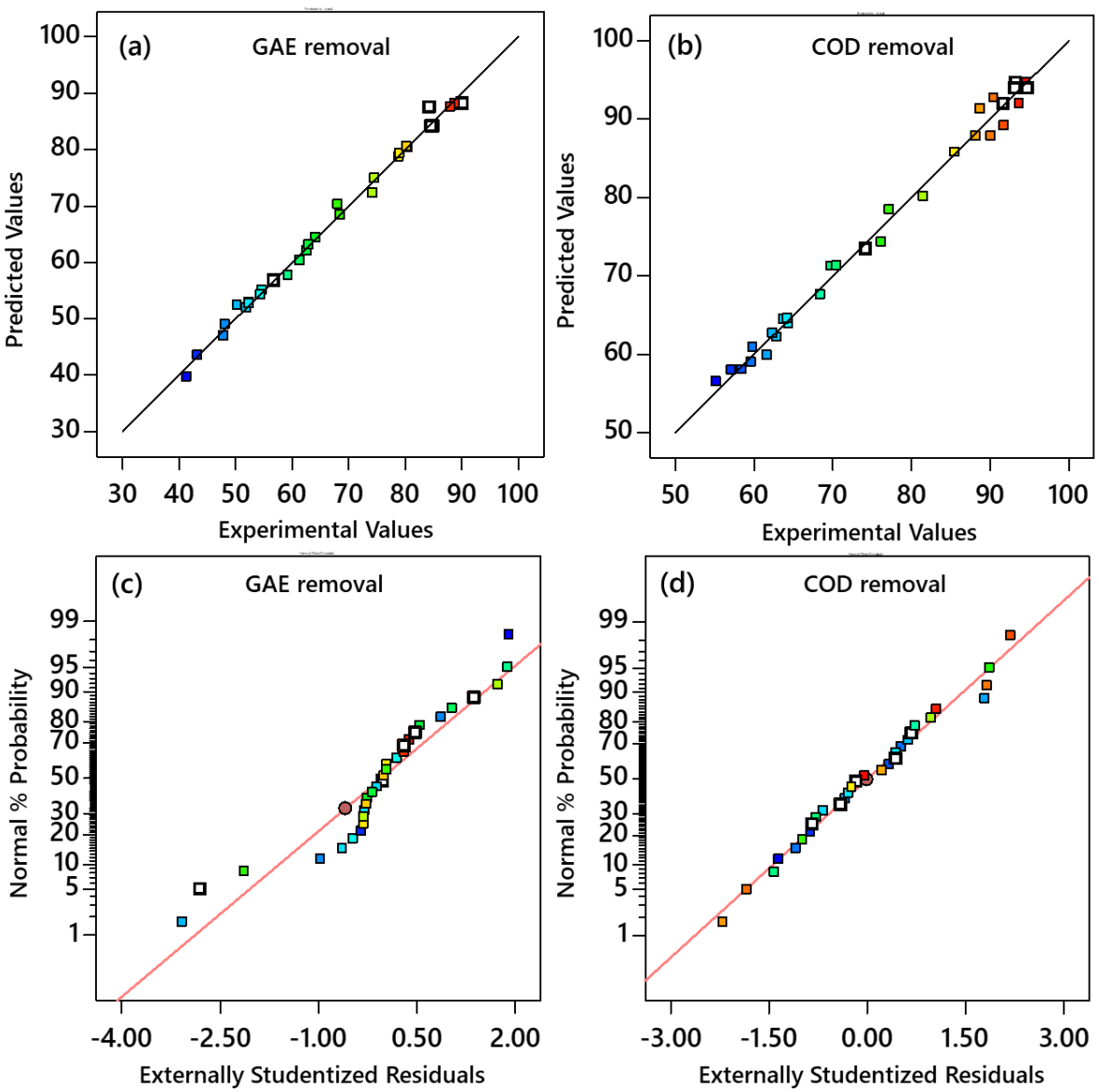

Fig. 10. Experimental and predicted values for (a) PCs as GAE removal and (b) COD removal and residuals Normal distribution plots for (c) PCs as GAE removal and (d) and COD removal.

To learn more about how well the model fit the data, the outcomes of 30 experiments that were designed using CCD in RSM were compared with predicted values as shown in Table 5. Table S4 presents the results of an ANOVA for the response surface quadratic models. The predicted values for PCs and COD removal are displayed in Fig.10(a) and (b), respectively, along with experimental values.

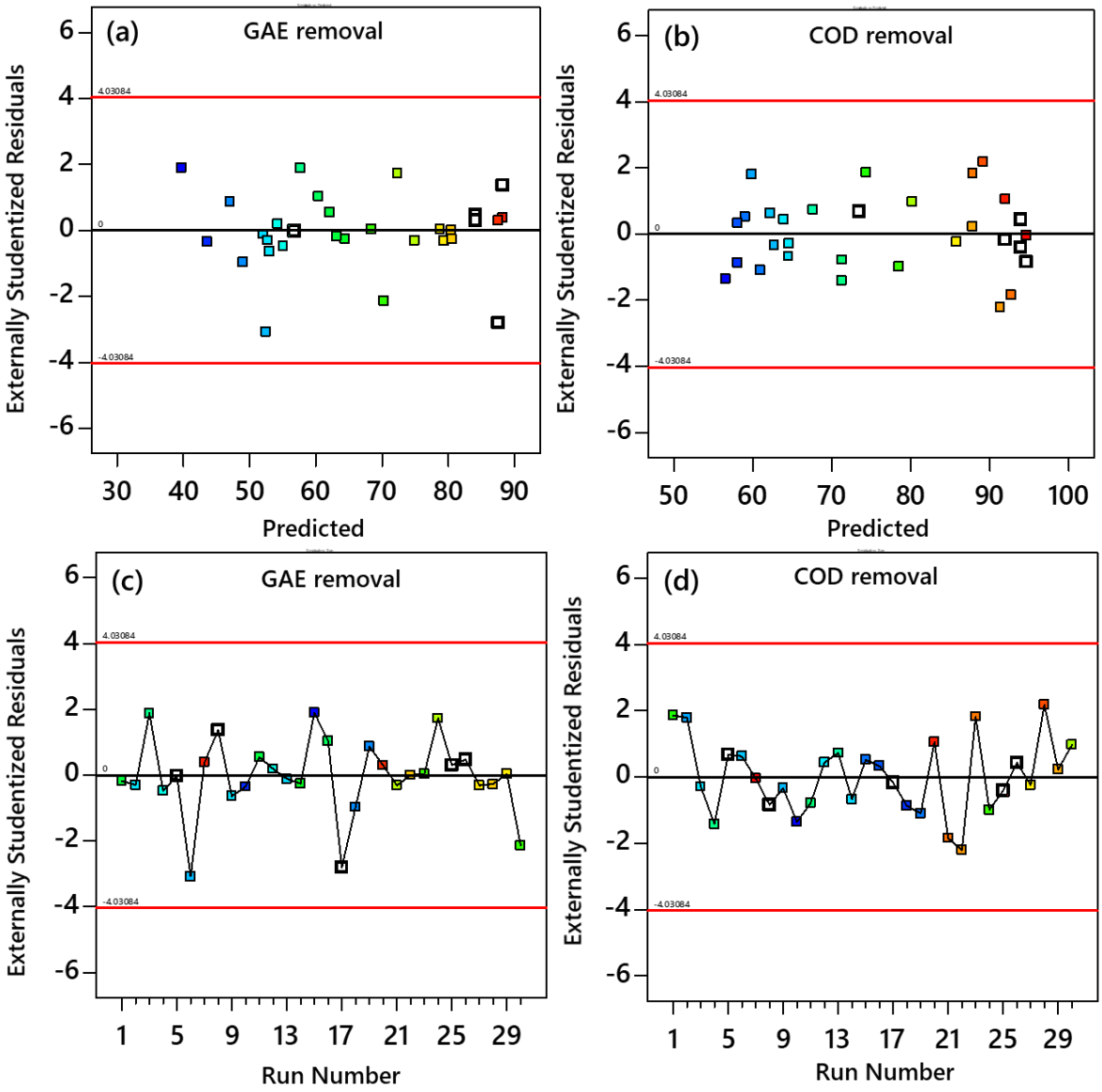

Fig. 11. Externally studentized residuals vs predicted values for (a) PCs removal and (b) COD removal, and externally studentized residuals vs run number for (c) PCs removal and (d) COD removal.

The distribution of the data points is fairly even, and they behave linearly. Plots show a reasonable level of agreement between the predicted and actual data. The fact that the predicted and experimental values were relatively close to one another suggests that the proposed empirical model is appropriate for predicting PCs and COD removal and displayed a reasonable level of agreement with the quadratic model. The residuals for the model for PCs and COD removal are depicted in Fig. 10(c) and (d) as having a normal distribution. The residual plots exhibit linear behavior as well as a straight line can be projected, indicating the accuracy of

model prediction. Fig. 11 presents the residual plots for the two models, PCs and COD removal. The residual vs. predicted values plots in Fig. 11(a) and (b) show that the residuals were distributed normally and random, which clearly indicates good model fitting. The residuals seem to have a normal distribution and be mostly random. Only two data points in Fig. 11(c) deviate from the Normal distribution, and they might not warrant further analysis.

3.4.2 Three-dimension view response surface and contour plots

The response surface can be used to identify a variety of independent variables that will maximise PC and COD photodegradation from TPOME. Maintaining the factors at their highest level could be very expensive, so keeping them within a range is frequently preferred for a process to be cost-effective. To optimize TiO_2 loading and H_2O_2 dosage for maximizing PCs removal, the response surface is plotted in Fig. 12(a). It is evident that the conditions with the maximum PCs removal efficiency (80–85%) were those with TiO_2 loadings between 0.7 and 1.12 g/L and H_2O_2 dosages between 0.03 and 0.065 mol/L. Similar to PCs removal, better COD removal efficiency (85–89%) displayed in Fig.13(a) was maintained when TiO_2 loading and H_2O_2 were within the same range. Fig. S4 displays the individual impact of these two factors on PCs and COD removal. Only the combined positive effects of TiO_2 loading and H_2O_2 dosage could have increased PCs and COD removal to the levels that were reached. This might be due to the synergistic interaction between TiO_2 and H_2O_2 that prevents photogenerated charges recombination by trapping the electron in the CB of TiO_2 and augmenting the amount of $^{\bullet}OH$ that TiO_2 produces when exposed to visible light (Álvarez et al., 2021). Therefore, more potent $^{\bullet}OH$ are available to attack the molecules of PCs and COD.

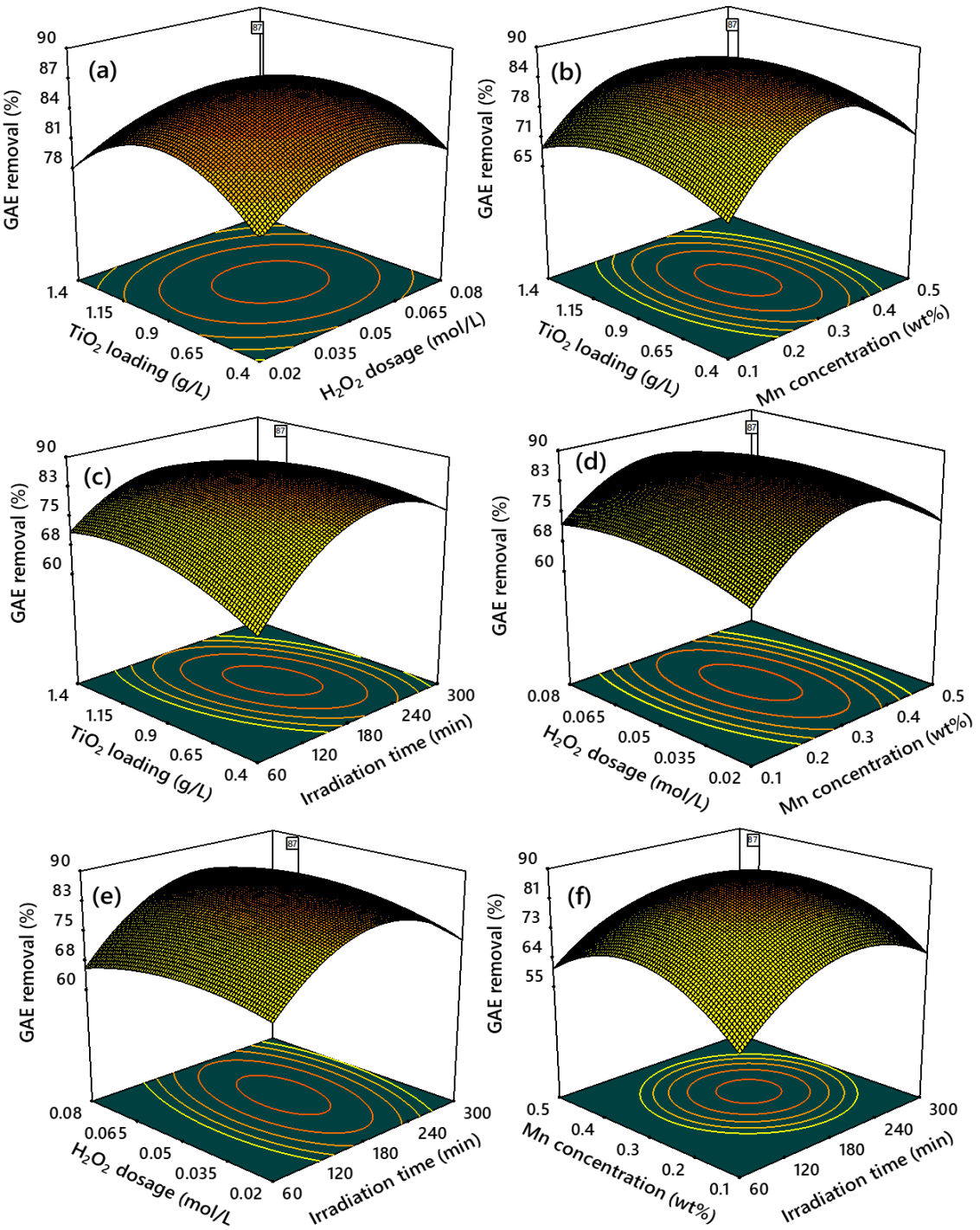

Fig. 12. Response surface plots of (a) TiO_2 loading va H_2O_2 dosage, (b) TiO_2 loading vs Mn concentration, (c) TiO_2 loading vs irradiation time, (d) H_2O_2 dosage vs Mn concentration, (e) H_2O_2 dosage vs irradiation time, and (f) Mn concentration vs irradiation time for PCs as GAE removal.

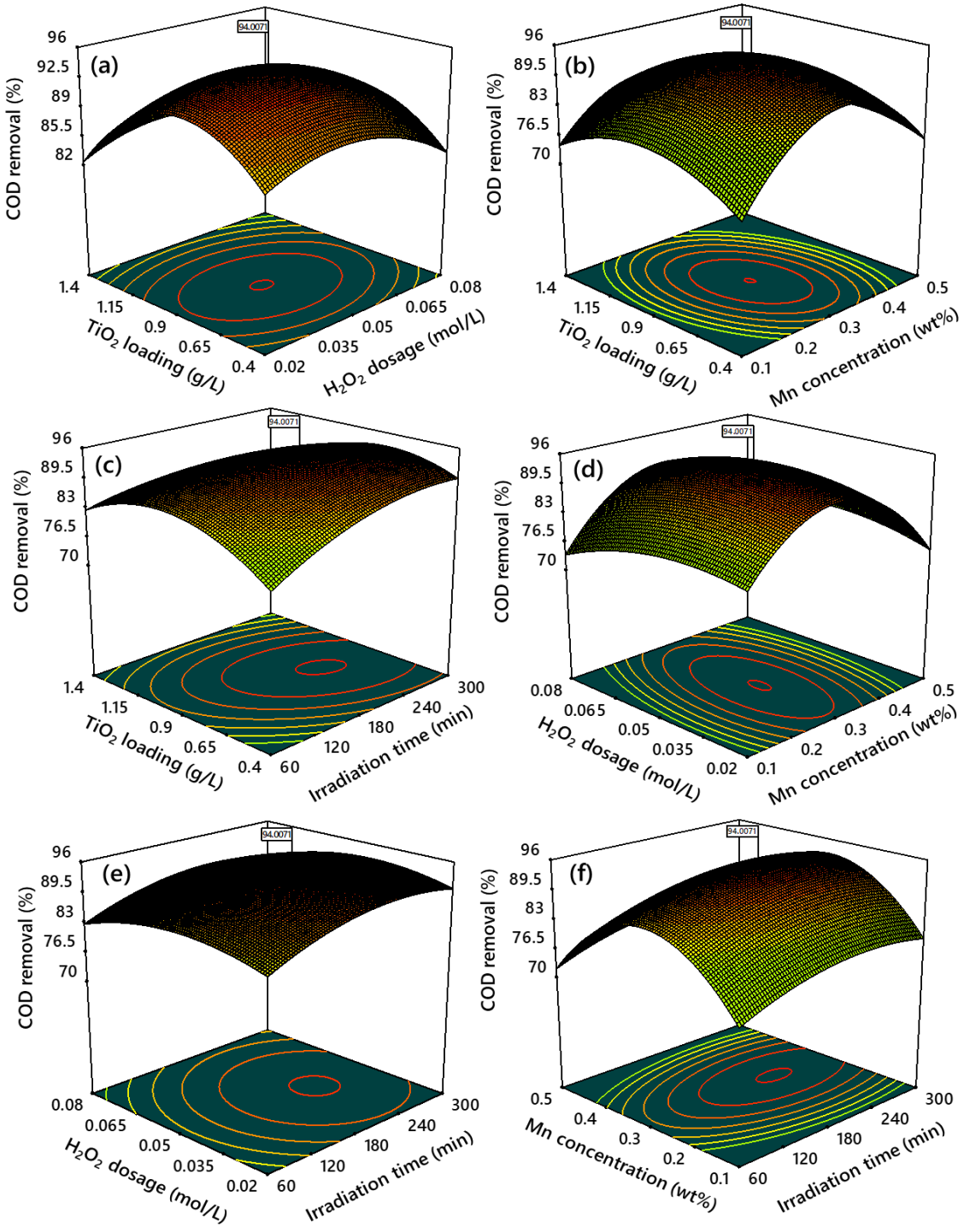

Fig. 13. Response surface plots of (a) TiO_2 loading va H_2O_2 dosage, (b) TiO_2 loading vs Mn concentration, (c) TiO_2 loading vs irradiation time, (d) H_2O_2 dosage vs Mn concentration, (e) H_2O_2 dosage vs irradiation time, and (f) Mn concentration vs irradiation time for COD removal.

To optimize TiO_2 loading and Mn concentration for maximizing PCs and COD removal, the response surface is plotted in Fig. 12(b) and Fig. 13(b), respectively. The maximum PCs removal (78−86%) was achieved at the TiO_2 loading of 0.7 and 1.12 g/L and Mn concentration

between 0.3−0.45wt%. Maximizing PCs and COD removal efficiency may require maintaining the Mn concentration in the optimum range. Because the Mn concentration has a significant impact on how well the Mn/TiO_2 performs in wastewater treatment applications (Ettireddy et al., 2007). If the Mn concentration is too low, the photocatalytic removal may be reduced because the bandgap may not be narrowed enough to produce an enhanced photoelectric effect under visible light and start photocatalytic reactions. High Mn concentrations caused the higher photocatalytic removal efficiency to lose effectiveness. This might be because there were too many crystal defects, which the photogenerated charge carriers may have used as recombination sites.

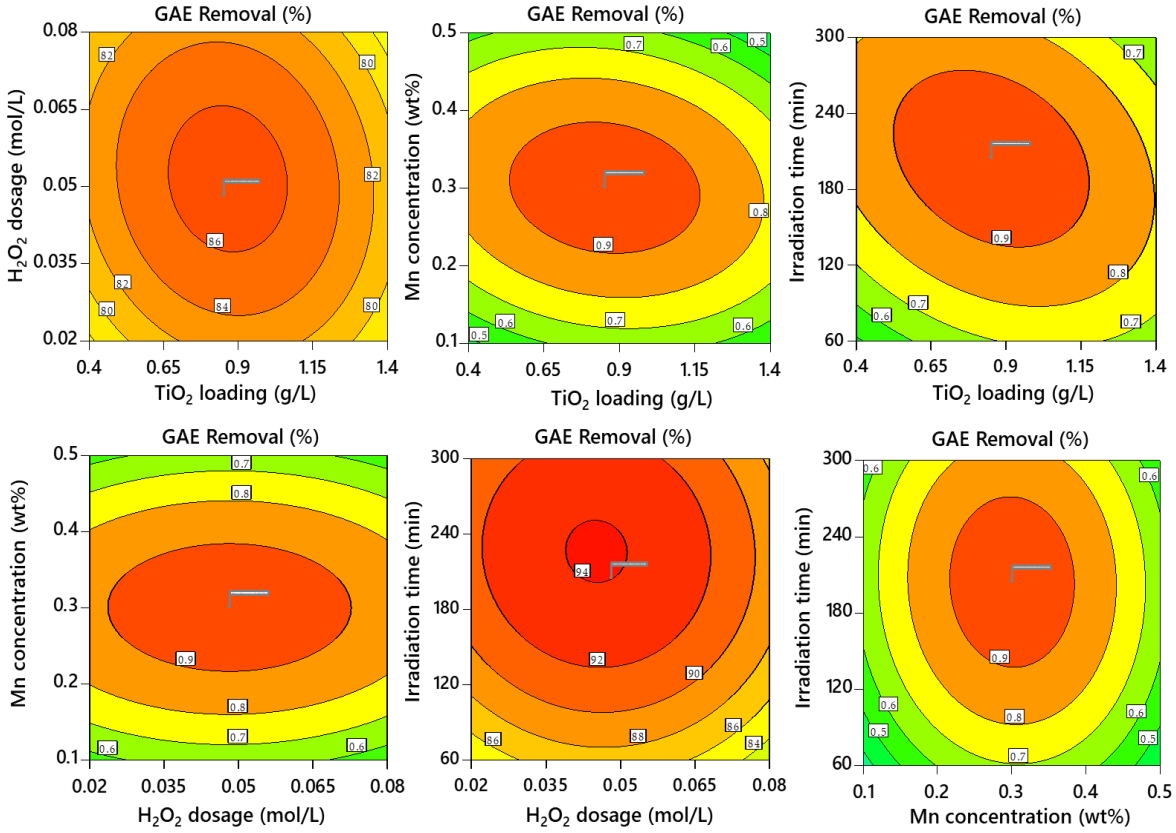

Fig. 14. Contour plots for phenolic compounds (as GAE) removal.

To optimize irradiation time for maximizing PCs and CODremoval, the response surface is plotted in Fig. 12(c) and Fig. 13(c), respectively. When the irradiation time was between 180 and 250 min, the best PCs and COD removal effeciency in the range of 75–88% were attained.

When the irraition time exceeded this range, the removal of both responses decreased, which might be caused by competition between the reactant and intermediate products as well as the deposition of byproducts results in the deactivation of active sites on the photocatalyst's surface (Pillai and Gupta, 2015). Fig. 12 and 13 show that the efficiency of removing PCs and COD begins to plateau, and that points farther away from the optimum perform worse. Due to exceeding and overshooting the optimum, the PCs and COD removal remained constant, if not even decreased, for two or three consecutive jumps. These characteristics led us to realise that the optimum has come into view.

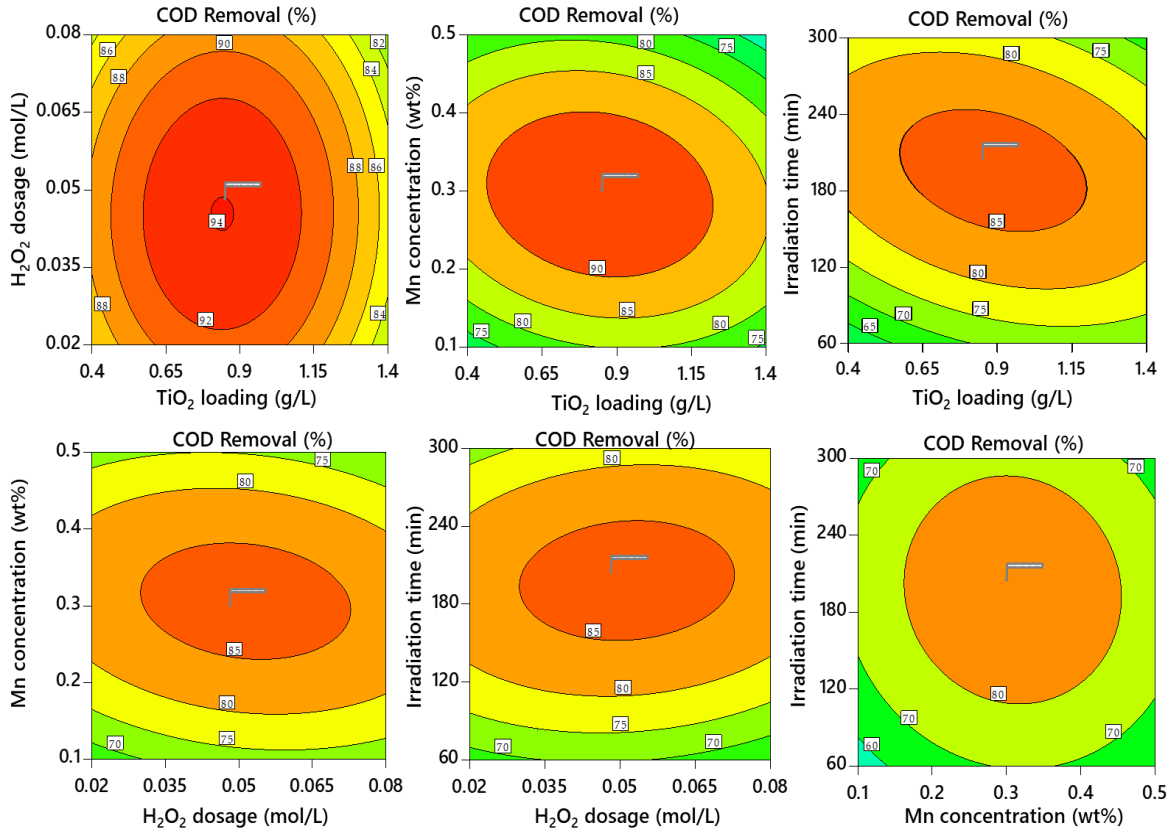

Fig. 15. Contour plots for COD (GAE) removal.

The ranges of the chosen independent factors can also be determined using the contour plot in order to achieve the same level of PCs and COD removal (responses, Y_1 and Y_2). For instance, the contour plots shown in Figs. 14 and 15 demonstrate that it is statistically possible to achieve the same level of PCs and COD removal for the same colour in the plot. For instance, the level of PCs and COD removal (80–90%) shown by the middle dark oval region of the

contour plot in Fig. 14 and 15 can be attained with TiO_2 loadings between 0.7 and 1.12 g/L, H_2O_2 dosages between 0.03 and 0.065 mol/L, Mn dosage 0.25 and 0.36wt%, and irradiation time between 140 and 260 min.

3.4.3 Perturbation plots

The effects of the chosen independent variables on PCs and COD removal were assessed using perturbation plots. By default, the Design Expert chose the independent variables' midpoint levels as the reference point. The perturbation plots in Fig. 16 were constructed to test the response variables' sensitivity to changes in the input variables. In order to identify a set of variables that meet the requirements set for each of them, the response is mapped by changing just one variable over its range while holding the others constant.

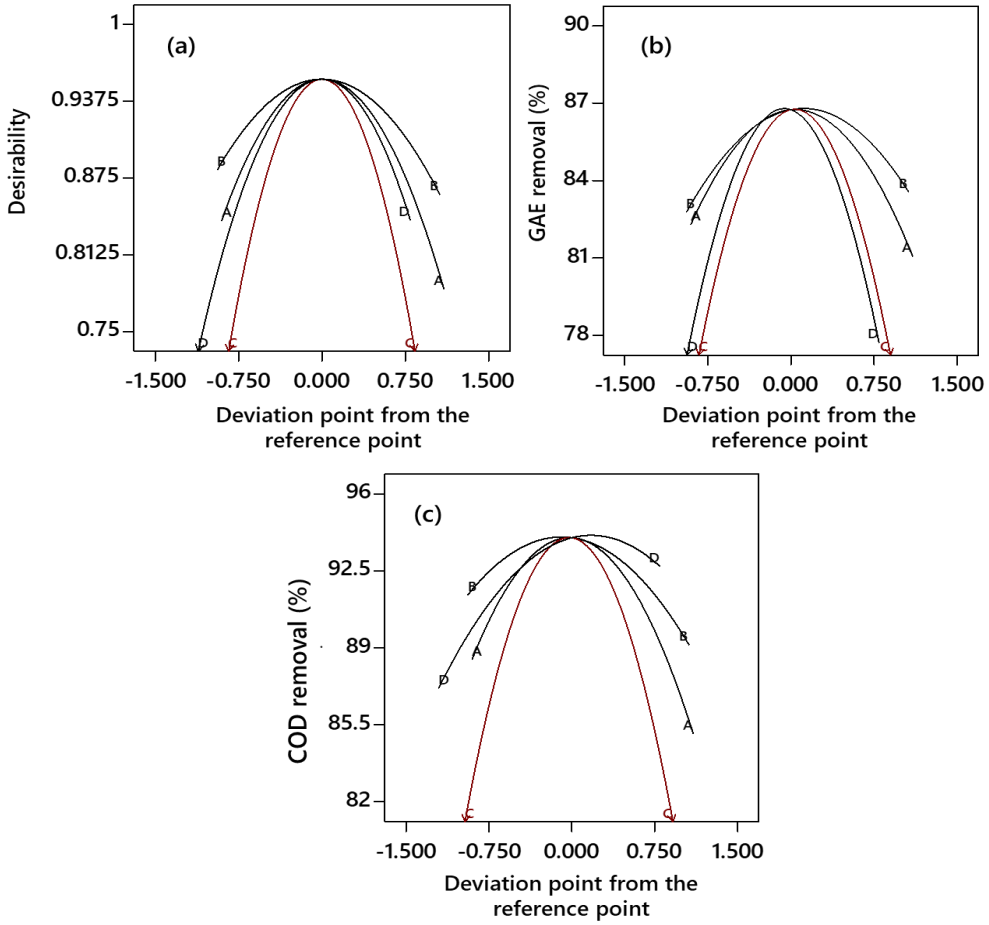

Fig. 16. Perturbation plots for (a) desirability, (a) PCs as GAE removal, and (c) COD removal.

As evidenced by a steeper curvature in the independent variables, both of the responses, PCs and COD removal, were sensitive to the change in selected independent variables (Morero et al., 2017). However, PCs removal responded differently to the independent variables than COD removal as shown in Fig.16(b). The change in TiO_2 loading, Mn concentration, and H_2O_2 dosage were found to affect the removal of COD more than they did the removal of PCs, which was more sensitive to Mn concentration and irradiation time. Perturbation plots with two analogous lines made it easy to explain the interaction between two-variables where the effects of one depend on the levels of the other variable. The removal of PCs and COD both increase as a result of the interaction, which is consistent with the 3D view response surface plots displayed in Fig. 13 and 14, respectively.

3.4.4 Experimental validation and numerical optimization

The 100% desirability function was chosen in numerical optimization to find the optimal set of parameters for the maximum photocatalytic removal of PCs and COD from TPOME. The goals for numerical optimization are listed in Table S5. The range of precise numbers was determined using the desirability values that were the closest to 1. By creating the best overlay plots, it was possible to visualise these simulated figures with multiple responses and the impact of independent variables on the responses (PCs as GAE and COD removal).

An important component of the RSM analysis was the adjustment in the desirability region when the variables varied within the selected ranges. This kind of research is helpful in determining the best operating parameters in light of the analysis's original conditions as well as the desired removal efficiency for PCs as GAE and COD removal from TPOME. By overlapping critical response, the overlay plot in Fig. 17 displays areas of desired response. In one optimum layered plot, the surface contours of the two responses were overlaid to create the simulated figures. The reasonable level constraints were chosen to be fairly similar to the acquired maximum removal efficiencies in order to obtain a moderately precise optimum zone

(Whitcomb and Anderson, 2004). According to the overlay plot, effective PCs and COD removal occurs at the optimal zone indicated by the yellow color shaded area. The optimum values for TiO_2 loading, H_2O_2 dosage, Mn concentration, and irradiation time are shown in Table 6 and were found to be 0.85 g/L, 0.048 mol/L, 0.301 wt.%, and 204 min, respectively.

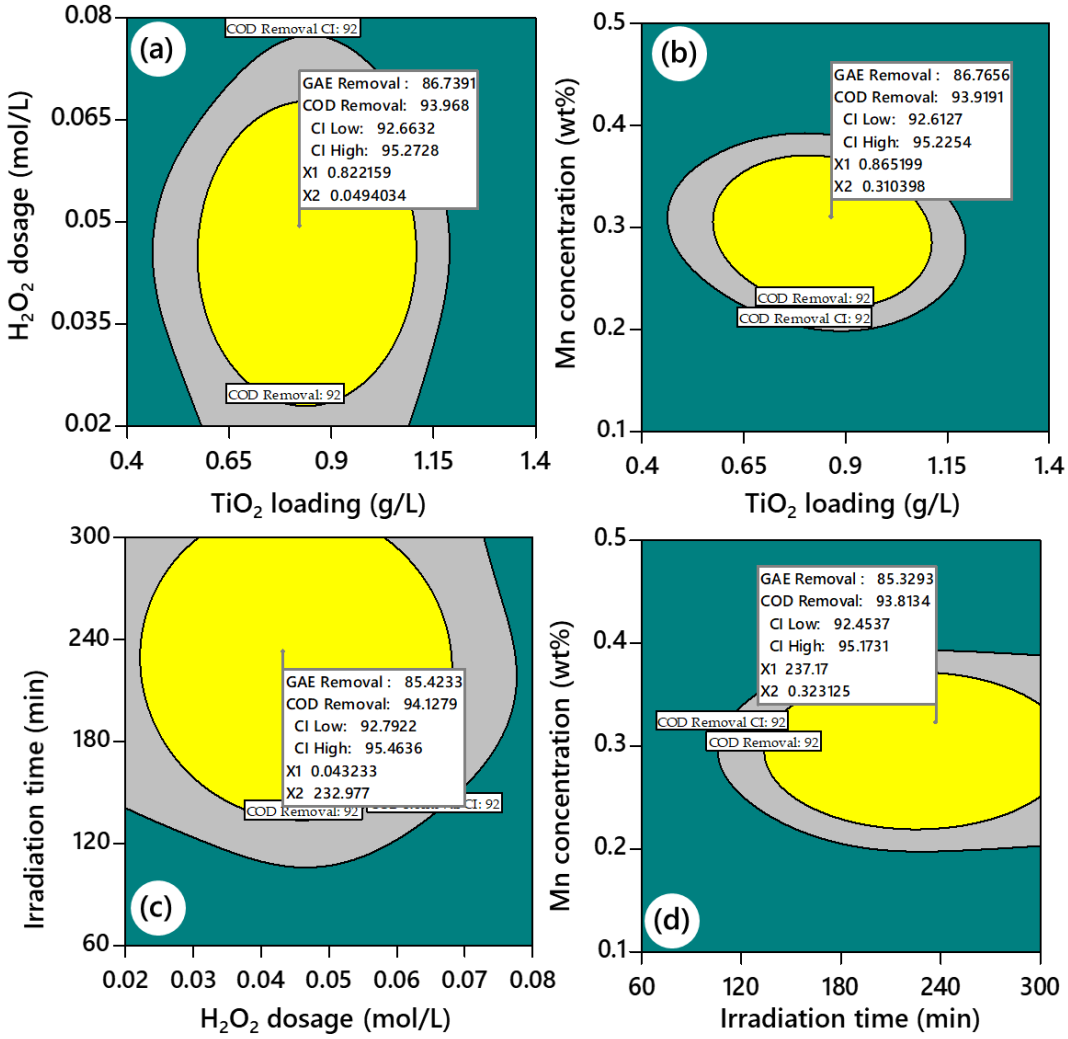

Fig. 17. Optimum overlay plot for (PCs as GAE) and COD removal.

The average of the four experimental runs at the optimal conditions for PCs and COD removal efficiency was 88.87 and 86.04%, respectively. These values fall within the ranges of 85.35–88.13 and 87.41–95.60 with a 95% confidence interval, demonstrating an excellent correlation with the predicted data. The values obtained should fall within the range predicted by the model with a 95% confidence interval for accurate results. The minimal difference

between predicted values and experimental results from laboratory tests for verification demonstrates the value of CCD/RSM as a tool for achieving best operating conditions for photocatalytic processes for PCs and COD removal from TPOME. The reliability of the results obtained is evidently demonstrated by the validation and verification. Table S7 is referred to for thorough numerical optimization statistics of PCs and COD removal.

Table 8 compares the photocatalysis used in this study with the previously researched technologies for remediating TPOME. Under the optimal conditions, the color removal efficiency was 62.76%, which is better than reported in the earlier studies. For instance, Tan et al. [57] investigated the photocatalytic procees for removing color from TPOME using the photocatalyst Degussa P-25. However, even under UVB irradiation, they could only remove 50% of the color from TPOME in 240 minutes. Surprisingly, in the current study, COD removal efficiency (88.87%) outperformed previously reported values for the sono-Fenton process of 80% (Taha and Ibrahim, 2014), 56% for photocatalysis using calcium ferrite as photocatalyst (Charles and Cheng, 2019), 16% for silver doped TiO_2 (Cheng et al., 2016), and 10% for platinum loaded TiO_2 (Cheng et al., 2015). The efficiency of PCs removal (86.04%) is much higher than that of earlier studies' findings and much quicker than the biological treatments under investigation so far. As shown in Table S8, the anaerobic digestion process could only remove 60–64% from initial 33 and 112 mg/L PCs in TPOME.

Table 6.

Optimum experimental conditions and their laboratory verification.

Independent variable	Symbol	Coded value	Unit	Removal (%)		Run	Removal (%)	
				PCs	COD		PCs	COD
TiO_2 loading	A	X_1	g/L	0.85	0.86	1	86.04	88.73
H_2O_2 dosage	B	X_2	mol/L	0.048	0.048	2	84.83	88.62
Mn concentration	C	X_3	wt.%	0.301	0.30	3	87.12	87.93
Irradiation time	D	X_4	min	204	202	4	86.17	90.22
Mean							86.04	88.87
σ							1.82	0.83

Monitoring the TOC removal allows to gauge the level of mineralization. Since the TOC concentration of the TPOME decreased by 84.66%, it is possible that PCs have been mineralized to some extent without the production of persistent intermediates. The efficiency of the TOC removal was a little lower than that of the PCs and COD removal, indicating that the organic removal might not be preferential to those two processes. The fact that TPOME had almost 62.81% of its color removed is significant because it shows that no extra intermediates or byproducts were created during the photocatalytic degradation process. The solution's yellow color is a common indicator of the presence of by-products from PC degradation and intermediate formation (Ayodhya et al., 2018). But in the present study, the final solution was clear and colorless, showing that the PCs had fully mineralized.

According to the findings, a highly effective and quick method for TPOME remediation that simultaneously reduces several pollution parameters, including phenolic compounds, COD, color, and TOC, is an improved photocatalytic method based on black TiO_2 that has had 0.3 weight percent Mn added. The aforementioned method holds great promise for the effective treatment of wastewater coming from the global palm oil industry's agricultural sector as well as other industries with high phenolic compound concentrations.

3.5 Recyclability of the M/BTiO_2 photocatalysts

Nanomaterial-containing treated effluents that are released into the environment may be toxic and harmful to biological systems (Clément et al., 2013). It is therefore necessary to recover them from the photoreactor to prevent environmental problems. Furthermore, their recovery is crucial because it determines how well the designed photocatalyst can be applied repeatedly in wastewater remediation and future applications. To assess the recyclability of our synthetic Mn/BTiO_2 photocatalyst, we used it for five consecutive cycles. The used Mn/BTiO_2 photocatalyst was removed from the TPOME suspension using centrifugation. After being thoroughly cleaned with water several times, this catalyst was dried for 24 hours at 60 °C before

being re-used to test its efficiency for PCs and COD removal in subsequent runs. The results for recyclability are shown in Fig. 18, which demonstrates a slight decline in the removal efficiency of PCs as GAE and COD from 86.04% and 88.87% to 78.38% and 79.92%, respectively, after the fifth repeated cycle. After the fifth cycle, the removal efficiency of COD and phenolic compounds, respectively, had standard deviations of 3.65% and 3.18%. PCs and COD removal efficiency decreased by 7.66% and 8.83%, respectively.

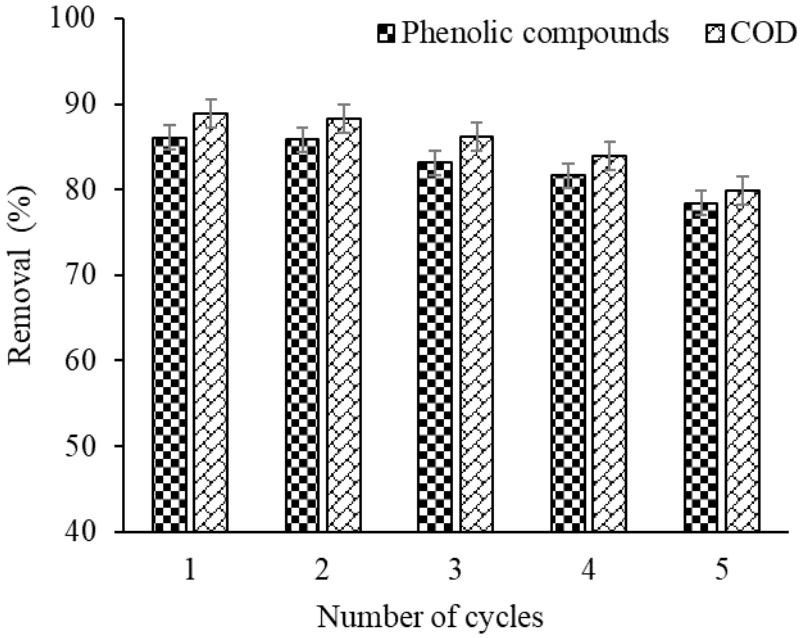

Fig. 18. Removal efficiency of PCs and COD by Mn/BTiO$_2$ photocatalyst at five consecutive cycles of 204 min.

The COD removal efficiency by $CaFe_2O_4$ (Charles and Cheng, 2019) and ZnO (Ng et al., 2017) decreased by 7% and 8.14% after the third repeated cycle, respectively, when the results are compared to those from earlier studies. It is therefore possible to draw the conclusion that the synthesized Mn/BTiO$_2$ used in the current study demonstrates extremely high performance and stability and can be used for the remediation of TPOME.

4. Conclusions

The current study assessed the efficacy of visible-light driven photocatalysis based on manganese modified black TiO_2 photocatalyst and addressed some significant process

limitations for remediating TPOME, particularly the removal of phenolic compounds and chemical oxygen demand. The black TiO_2 was produced in glycerol and calcination at 300°C for one hour to give it improved physicochemical and semiconducting properties as well performance for the removal of phenolic compounds (48%). With additional Mn modification, the black TiO_2 that was performing the best under non-optimized conditions, phenolic compound removal was further increased to 60.12%. The removal of phenolic compounds along with COD was improved by optimizing the independent factor to 86.04% and 88.87%, respectively. High reliability in the estimation of phenolic compound and COD removal was indicated by the statistical analysis, which showed high R^2 and lower MSE, RMSE, and MAPE for both the response variables, phenolic compounds. Additionally, the optimized process was successful in removing 62.76% color and 84.66% TOC from TPOME. The results of this study confirm that the improved photocatalytic process, which uses Mn modified black TiO_2 that responds to visible light, is an effective method for polishing TPOME, particularly for removing phenolic compounds and chemical oxygen demand. The lower TOC value following the treatment shows that the aforementioned process also ensures complete mineralization of phenolic compounds with minimal intermediate formation.

Acknowledgements

The authors sincerely appreciate funding from Researchers Supporting Project number [RSP-2023R399], King Saud University, Riyadh, Saudi Arabia. Technical and logistic support from the PMAS-AAUR is highly acknowledged.

Funding sources

The authors sincerely appreciate funding from Researchers Supporting Project number [RSP-2023R399], King Saud University, Riyadh, Saudi Arabia.

Author credit statement

Rab Nawaz: Conceptualization, Methodology, Investigations, Formal analysis, Visualization, Writing-Original draft preparation, Writing- Reviewing and Editing. **Sajjad Haider:** Funding acquisition, Data curation, Project administration, Supervision, Resources, Writing-Reviewing and Editing. **Muzammil Anjum:** Supervision; Validation, Writing-Reviewing and Editing. **Vipin Kumar Oad**: Investigation; Methodology; Writing- Reviewing and Editing. **Adnan Haider:** Writing- Reviewing and Editing, Formal analysis, Supervision. **Rawaiz Khan:** Investigations, Writing- Reviewing and Editing. **Muhammad Aqif:** Methodology, Writing-Original draft. **Tahir Haneef:** Investigations; Writing-Reviewing and Editing. **Nasruulah Khan:** Formal analysis, Data curation and validation, Writing-Reviewing and Editing

References

Ahmad, A., Ismail, S., Bhatia, S., 2005. Optimization of coagulation−flocculation process for palm oil mill effluent using response surface methodology. Environ. Sci. Technol. 39, 2828-2834. https://doi.org/10.1021/es0498080.

Alhaji, M.H., Sanaullah, K., Salleh, S.F., Baini, R., Lim, S.F., Rigit, A.R.H., Said, K.A.M., Khan, A., 2018. Photo-oxidation of pre-treated palm oil mill Effluent using cylindrical column immobilized photoreactor. Process Saf. Environ. Prot. 117, 180-189. https://doi.org/10.1016/j.psep.2018.04.012.

Álvarez, M.A., Ruidíaz-Martínez, M., Rivera-Utrilla, J., Sánchez-Polo, M., López-Ramón, M.V., 2021. Effect of operational parameters on photocatalytic degradation of ethylparaben using rGO/TiO_2 composite under UV radiation. Environ. Res. 200, 111750. https://doi.org/10.1016/j.envres.2021.111750.

Aris, A., Jusoh, M.N.H., Wahab, N.S.A.A. 2019. Applications of Advanced Oxidation Processes in Palm Oil Mill Effluent Treatment. Advanced Oxidation Processes (AOPs) in Water and Wastewater Treatment. IGI Global. 10.4018/978-1-5225-5766-1.ch006.

Ateia, M., Alalm, M.G., Awfa, D., Johnson, M.S., Yoshimura, C., 2020. Modeling the degradation and disinfection of water pollutants by photocatalysts and composites: A critical review. Sci. Total Environ. 698, 134197. https://doi.org/10.1016/j.scitotenv.2019.134197.

Ayodhya, D., Perka, S., Nambigari, N., 2018. Sunlight-driven efficient photocatalytic and antimicrobial studies of microwave-assisted Ir-doped TiO_2 nanoparticles for environmental safety. Nanochem. Res. 3, 36-49. 10.22036/NCR.2018.01.005.

Bello, M.M., Abdul Raman, A.A., 2017. Trend and current practices of palm oil mill effluent polishing: Application of advanced oxidation processes and their future perspectives. J. Environ. Manage. 198, 170-182. https://doi.org/10.1016/j.jenvman.2017.04.050.

Bhardwaj, S., Pal, B., 2020. Solar light driven photocatalytic oxidative degradation of methyl viologen using Mn^{2+}/Mn^{7+}-TiO_2 nanocomposites. J. Photochem. Photobiol. A: Chem. 393, 112430. https://doi.org/10.1016/j.jphotochem.2020.112430.

Bharti, B., Kumar, S., Lee, H.N., Kumar, R., 2016. Formation of oxygen vacancies and Ti^{3+} state in TiO_2 thin film and enhanced optical properties by air plasma treatment. Sci. Rep. 6, 32355. https://doi.org/10.1038/srep32355.

Bi, X., Du, G., Sun, D., Zhang, M., Yu, Y., Su, Q., Ding, S., XU, B., 2020. Room-temperature synthesis of yellow TiO_2 nanoparticles with enhanced photocatalytic properties. Appl. Surf. Sci. 511, 145617. https://doi.org/10.1016/j.apsusc.2020.145617.

Bousiakou, L. G., Dobson, P. J., Jurkin, T., Marić, I., Aldossary, O., Ivanda, M., 2022. Optical, structural and semiconducting properties of Mn doped TiO_2 nanoparticles for cosmetic applications. J. King Saud Univ. Sci. 34, 101818. https://doi.org/10.1016/j.jksus.2021.101818.

Charles, A., Cheng, C.K., 2019. Photocatalytic treatment of palm oil mill effluent by visible light-active calcium ferrite: Effects of catalyst preparation technique. J. Environ. Manage. 234, 404-411. https://doi.org/10.1016/j.jenvman.2019.01.024.

Chen, L.Y., Cheng, C.W., Liang, J.Y., 2015. Effect of esterification condensation on the Folin–Ciocalteu method for the quantitative measurement of total phenols. Food Chem. 170, 10-15. https://doi.org/10.1016/j.foodchem.2014.08.038.

Cheng, C.K., Deraman, M.R., Ng, K.H., Khan, M.R., 2016. Preparation of titania doped argentum photocatalyst and its photoactivity towards palm oil mill effluent degradation. J. Clean. Prod. 112, 1128-1135. https://doi.org/10.1016/j.jclepro.2015.06.104.

Cheng, C.K., Rizauddin Derahman, M., Khan, M.R., 2015. Evaluation of the photocatalytic degradation of pre-treated palm oil mill effluent (POME) over Pt-loaded titania. J. Environ. Chem. Eng. 3, 261-270. https://doi.org/10.1016/j.jece.2014.10.016.

Cheng, Y.W., Chong, C.C., Lam, M.K., Ayoub, M., Cheng, C.K., Lim, J.W., Yusup, S., Tang, Y., Bai, J., 2021. Holistic process evaluation of non-conventional palm oil mill effluent (POME) treatment technologies: A conceptual and comparative review. J. Hazard. Mater. 409, 124964. https://doi.org/10.1016/j.jhazmat.2020.124964.

Chia, W.Y., Chong, Y.Y., Chew, K.W., Vimali, E., Jayaram, M., Selvarajoo, A., Muthuvelu, K.S., Varalakshmi, P., Show, P.L., Arumugasamy, S.K., 2020. Outlook on biorefinery potential of palm oil mill effluent for resource recovery. J. Environ. Chem. Eng. 8, 104519. https://doi.org/10.1016/j.jece.2020.104519.

Choi, A.Y., Han, C.H., 2014. A study on the band gap and the doping level of V-doped TiO_2 with respect to the visible-light photocatalytic activity. J. Nanosci. Nanotechnol. 14, 8070-8073. https://doi.org/10.1166/jnn.2014.9469.

Choi, J., Park, H., Hoffmann, M.R., 2010. Effects of single metal-ion doping on the visible-light photoreactivity of TiO_2. J. Phys. Chem. C. 114, 783-792. https://doi.org/10.1021/jp908088x.

Choi, W., Termin, A., Hoffmann, M.R., 2002. The role of metal ion dopants in quantum-sized TiO_2: correlation between photoreactivity and charge carrier recombination dynamics. J. Phys. Chem. B. 98, 13669-13679. https://doi.org/10.1021/j100102a038.

Chowdhury, P., Nag, S., Ray, A.K., 2017. Degradation of phenolic compounds through UV and visible-light-driven photocatalysis: technical and economic aspects. Phenolic Compounds: Natural Sources, Importance. Intech. 16:395-417. http://dx.doi.org/10.5772/66134.

Clément, L., Hurel, C., Marmier, N., 2013. Toxicity of TiO_2 nanoparticles to cladocerans, algae, rotifers and plants–Effects of size and crystalline structure. Chemosphere, 90, 1083-1090. https://doi.org/10.1016/j.chemosphere.2012.09.013.

Deng, Q., Xia, X., Guo, M., Gao, Y., Shao, G., 2011. Mn-doped TiO_2 nanopowders with remarkable visible light photocatalytic activity. Mater. Lett. 65, 2051-2054. https://doi.org/10.1016/j.matlet.2011.04.010.

Ettireddy, P. R., Ettireddy, N., Mamedov, S., Boolchand, P., Smirniotis, P.G., 2007. Surface characterization studies of TiO_2 supported manganese oxide catalysts for low temperature SCR of NO with NH_3. Appl. Catal. B: Environ. 76, 123-134. https://doi.org/10.1016/j.apcatb.2007.05.010.

Glaz, B., Yeater, K.M., 2020. Applied statistics in agricultural, biological, and environmental sciences, John Wiley & Sons, Madison, WI 53711-58011 USA.

Iskandar, M.J., Baharum, A., Anuar, F.H., Othaman, R., 2018. Palm oil industry in South East Asia and the effluent treatment technology–A review. Environ. Technol. Innov. 9, 169-185. https://doi.org/10.1016/j.eti.2017.11.003.

Jiang, Z., Hu, J., Zhang, X., Zhao, Y., Fan, X., Zhong, S., Zhang, H., Yu, X., 2020. A generalized predictive model for TiO_2–Catalyzed photo-degradation rate constants of water contaminants through artificial neural network. Environ. Res. 187, 109697. https://doi.org/10.1016/j.envres.2020.109697.

Kamyab, H., Yuzir, M.A., Riyadi, F.A., Ostadrahimi, A., Khademi, T., Ghfar, A.A., Kirpichnikova, I., 2022. Electrochemical oxidation of palm oil mill effluent using platinum as anode: Optimization using response surface methodology. Environ. Res. 214, 113993. https://doi.org/10.1016/j.envres.2022.113993.

Khraisheh, M., Wu, L., Ala'A, H., Albadarin, A.B., Walker, G.M., 2012. Phenol degradation by powdered metal ion modified titanium dioxide photocatalysts. Chem. Eng. J. 213, 125-134. https://doi.org/10.1016/j.cej.2012.09.108.

Kong, L., Wang, C., Zheng, H., Zhang, X., Liu, Y., 2015. Defect-induced yellow color in Nb-doped TiO_2 and its impact on visible-light photocatalysis. J. Phys. Chem. C. 119, 16623-16632. https://doi.org/10.1021/acs.jpcc.5b03448.

Kouhail, M., Benayada, A., Gmouh, S., 2022. Preparation and Characterization of Black Titanium by Chemical Reduction of TiO_2 and its Photocatalytic Activity. Curr. Nanosci. 18, 391-398. https://doi.org/10.2174/1573413717666210826125835.

Kunnamareddy, M., Ganesan, S., Hatamleh, A.A., Alnafisi, B.K., Rajendran, R., Chinnasamy, R., Arumugam, P., Diravidamani, B., Lo, H.M., 2023. Enhancement in the visible light induced photocatalytic and antibacterial properties of titanium dioxide codoped with cobalt and sulfur. Environ. Res. 216, 114705. https://doi.org/10.1016/j.envres.2022.114705.

Liang, Y., Huang, G., Xin, X., Yao, Y., Li, Y., Yin, J., Li, X., Wu, Y., Gao, S., 2021. Black titanium dioxide nanomaterials for photocatalytic removal of pollutants: a review. J. Mater. Sci. Technol. 112, 239-262. https://doi.org/10.1016/j.jmst.2021.09.057.

Liang, Y., Shao, G., 2019. First principles study for band engineering of $KNbO_3$ with 3d transition metal substitution. RSC Adv. 9, 7551-7559. 10.1039/C9RA00289H.

Lu, L., Xia, X., Luo, J., Shao, G., 2012. Mn-doped TiO_2 thin films with significantly improved optical and electrical properties. J. Phys. D: Appl. Phys. 45, 485102. 10.1088/0022-3727/45/48/485102.

Miklos, D.B., Remy, C., Jekel, M., Linden, K.G., Drewes, J.E., Hübner, U., 2018. Evaluation of advanced oxidation processes for water and wastewater treatment–A critical review. Water Res. 139, 118-131. https://doi.org/10.1016/j.watres.2018.03.042.

Moradeeya, P. G., Sharma, A., Kumar, M.A., Basha, S., 2022. Titanium dioxide based nanocomposites – Current trends and emerging strategies for the photocatalytic degradation of ruinous environmental pollutants. Environ. Res. 204, 112384. https://doi.org/10.1016/j.envres.2021.112384.

Morero, B., Groppelli, E.S., Campanella, E.A., 2017. Evaluation of biogas upgrading technologies using a response surface methodology for process simulation. J. Clean. Prod. 141, 978-988. https://doi.org/10.1016/j.jclepro.2016.09.167.

Moya, A., Cherevan, A., Marchesan, S., Gebhardt, P., Prato, M., Eder, D., Vilatela, J.J., 2015. Oxygen vacancies and interfaces enhancing photocatalytic hydrogen production in mesoporous CNT/TiO_2 hybrids. Appl. Catal. B: Environ. 179, 574-582. https://doi.org/10.1016/j.apcatb.2015.05.052.

Nawaz, R., Kait, C.F., Chia, H.Y., Isa, M.H., Huei, L.W., Sahrin, N.T., Khan, N., 2021. Countering major challenges confronting photocatalytic technology for the remediation of treated palm oil mill effluent: A review. Environ. Technol. Innov. 23, 101764. https://doi.org/10.1016/j.eti.2021.101764.

Ng, K.H., 2021. Adoption of TiO_2-photocatalysis for palm oil mill effluent (POME) treatment: Strengths, weaknesses, opportunities, threats (SWOT) and its practicality against traditional treatment in Malaysia. Chemosphere, 270, 129378. https://doi.org/10.1016/j.chemosphere.2020.129378.

Ng, K.H., Cheng, Y.W., Khan, M.R., Cheng, C.K., 2016a. Optimization of photocatalytic degradation of palm oil mill effluent in UV/ZnO system based on response surface methodology. J. Environ. Manage. 184, 487-493. https://doi.org/10.1016/j.jenvman.2016.10.034.

Ng, K.H., Gan, Y.S., Cheng, C.K., Liu, K.H., Liong, S.T., 2020. Integration of machine learning-based prediction for enhanced Model's generalization: Application in

photocatalytic polishing of palm oil mill effluent (POME). Environ. Pollut. 267, 115500. https://doi.org/10.1016/j.envpol.2020.115500.

Ng, K.H., Khan, M.R., Ng, Y.H., Hossain, S.S., Cheng, C.K., 2017. Restoration of liquid effluent from oil palm agroindustry in Malaysia using UV/TiO_2 and UV/ZnO Photocatalytic systems: A comparative study. J. Environ. Manage.196, 674-680. https://doi.org/10.1016/j.jenvman.2017.03.078.

Ng, K.H., Lee, C.H., Khan, M.R., Cheng, C.K., 2016b. Photocatalytic degradation of recalcitrant POME waste by using silver doped titania: Photokinetics and scavenging studies. Chem. Eng. J. 286, 282-290. https://doi.org/10.1016/j.cej.2015.10.072.

Pan, X., Yang, M.Q., Fu, X., Zhang, N., Xu, Y.J., 2013. Defective TiO_2 with oxygen vacancies: synthesis, properties and photocatalytic applications. Nanoscale, 5, 3601-3614. https://doi.org/10.1039/C3NR00476G.

Piątkowska, A., Janus, M., Szymański, K., Mozia, S., 2021. C-, N-and S-Doped TiO_2 Photocatalysts: A Review. Catalysts, 11, 144. https://doi.org/10.3390/catal11010144.

Pillai, I.M.S., Gupta, A.K., 2015. Batch and continuous flow anodic oxidation of 2,4-dinitrophenol: Modeling, degradation pathway and toxicity. J. Electroanal. Chem. 756, 108-117. https://doi.org/10.1016/j.jelechem.2015.08.020.

Qiu, J., Zeng, G., Ge, M., Arab, S., Mecklenburg, M., Hou, B., Shen, C., Benderskii, A.V., Cronin, S.B., 2016. Correlation of Ti^{3+} states with photocatalytic enhancement in TiO_2-passivated p-GaAs. J. Catal. 337, 133-137. https://doi.org/10.1016/j.jcat.2016.02.002.

Rostami, M., Badiei, A., Ganjali, M.R., Rahimi-Nasrabadi, M., Naddafi, M., Karimi-Maleh, H., 2022. Nano-architectural design of TiO_2 for high performance photocatalytic degradation of organic pollutant: A review. Environ. Res. 212, 113347. https://doi.org/10.1016/j.envres.2022.113347.

Saeed, M.O., Azizli, K., Isa, M.H., Bashir, M.J.K. 2015. Application of CCD in RSM to obtain optimize treatment of POME using Fenton oxidation process. J. Water Process. Eng. 8, e7-e16. https://doi.org/10.1016/j.jwpe.2014.11.001.

Sharotri, N., Sharma, D., Sud, D., 2019. Experimental and theoretical investigations of Mn-N-co-doped TiO_2 photocatalyst for visible light induced degradation of organic pollutants. J. Mater. Res. Technol. 8, 3995-4009. https://doi.org/10.1016/j.jmrt.2019.07.008.

Shvab, R., Hryha, E.. Nyborg, L., 2017. Surface chemistry of the titanium powder studied by XPS using internal standard reference. Powder Metall. 60, 42-48. https://doi.org/10.1080/00325899.2016.1271092.

Sigcha-Pallo, C., Peralta-Hernández, J.M., Alulema-Pullupaxi, P., Carrera, P., Fernández, L., Pozo, P., Espinoza-montero, P.J., 2022. Photoelectrocatalytic degradation of diclofenac with a boron-doped diamond electrode modified with titanium dioxide as a photoanode. Environ. Res. 212, 113362. https://doi.org/10.1016/j.envres.2022.113362.

Sin, J.C., Chin, Y.H., Lam, S.M., 2019. WO_3/Nb_2O_5 nanoparticles-decorated hierarchical porous ZnO microspheres for enhanced photocatalytic degradation of palm oil mill effluent and simultaneous production of biogas. Trans Tech Publ, 379-385. https://doi.org/10.4028/www.scientific.net/KEM.821.379.

Sin, J.C., Lam, S.M., Zeng, H., Lin, H., Li, H., Mohamed, A.R., 2020a. Constructing magnetic separable $BiOBr/MnFe_2O_4$ as efficient Z-scheme nanocomposite for visible light-driven degradation of palm oil mill effluent and inactivation of bacteria. Mater. Lett. 275, 128112. https://doi.org/10.1016/j.matlet.2020.128112.

Sin, J.C., Lim, C.A., Lam, S.M., Zeng, H., Lin, H., Li, H., Mohamed, A.R., 2020b. Fabrication of novel visible light-driven Nd-doped BiOBr nanosheets with enhanced photocatalytic performance for palm oil mill effluent degradation and Escherichia coli inactivation. J. Phys. Chem. Solids. 140, 109382. https://doi.org/10.1016/j.jpcs.2020.109382.

Sun, M., Fang, L.M., Hong, X.H., Zhang, F., Zhai, L.F., 2020. Catalytic behaviors of manganese oxides in electro-assisted catalytic air oxidation reaction: Influence of structural properties. Appl. Surf. Sci. 145536. https://doi.org/10.1016/j.apsusc.2020.145536.

Taha, M., Ibrahim, A., 2014. Characterization of nano zero-valent iron (nZVI) and its application in sono-Fenton process to remove COD in palm oil mill effluent. J. Environ. Chem. Eng. 2, 1-8. https://doi.org/10.1016/j.jece.2013.11.021.

Tian, M., Mahjouri-Samani, M., Eres, G., Sachan, R., Yoon, M., Chisholm, M.F., Wang, K., Puretzky, A.A., Rouleau, C.M., Geohegan, D.B., 2015. Structure and formation mechanism of black TiO_2 nanoparticles. ACS Nano, 9, 10482-10488. https://doi.org/10.1021/acsnano.5b04712.

Ullattil, S.G., Periyat, P., 2015. Green microwave switching from oxygen rich yellow anatase to oxygen vacancy rich black anatase TiO_2 solar photocatalyst using Mn (ii) as 'anatase phase purifier'. Nanoscale, 7, 19184-19192. https://doi.org/10.1039/C5NR05975E.

Whitcomb, P.J., Anderson, M.J., 2004. RSM simplified: optimizing processes using response surface methods for design of experiments, Taylor & Francis. https://doi.org/10.1201/9781315382326.

Wong, K.A., Lam, S.M., Sin, J.C., 2019. Wet chemically synthesized ZnO structures for photodegradation of pre-treated palm oil mill effluent and antibacterial activity. Ceram. Int. 45, 1868-1880. https://doi.org/10.1016/j.ceramint.2018.10.078.

Wu, T., Englehardt, J.D., 2012. A new method for removal of hydrogen peroxide interference in the analysis of chemical oxygen demand. Environ. Sci. Technol., 46, 2291-2298. https://doi.org/10.1021/es204250k.

Xia, T., Chen, X., 2013. Revealing the structural properties of hydrogenated black TiO_2 nanocrystals. J. Mater. Chem. A. 1, 2983-2989. https://doi.org/10.1039/C3TA01589K.

Xia, X., Lu, L., Walton, A., Ward, M., Han, X., Brydson, R., Luo, J., Shao, G., 2012. Origin of significant visible-light absorption properties of Mn-doped TiO_2 thin films. Acta Materialia. 60, 1974-1985. https://doi.org/10.1016/j.actamat.2012.01.006.

Yang, Y., Liu, G., Irvine, J.T., Cheng, H. M. 2016. Enhanced photocatalytic H_2 production in core–shell engineered rutile TiO_2. Adv. Mater., 28, 5850-5856. https://doi.org/10.1002/adma.201600495.

Zhang, F., Feng, G., Hu, M., Huang, Y., Zeng, H. 2020. Liquid-Plasma Hydrogenated Synthesis of Gray Titania with Engineered Surface Defects and Superior Photocatalytic Activity. Nanomaterials. 10, 342. https://doi.org/10.3390/nano10020342.

Zhang, Y., Zhang, Y., Huang, Y., Jia, Y., Chen, L., Pan, Y., Wang, M. 2021. Adsorptive-photocatalytic performance and mechanism of Me (Mn,Fe)-N co-doped TiO_2/SiO_2 in cyanide wastewater. J. Alloys Compd. 867, 159020. https://doi.org/10.1016/j.jallcom.2021.159020.